

University of Massachusetts Amherst

**ScholarWorks@UMass Amherst**

---

Chemical Engineering Faculty Publication  
Series

Chemical Engineering

---

2020

## **Plasmonic hot electrons for sensing, photodetection, and solar energy applications: A perspective**

Haibin Tang

Chih-Jung Chen

Zhulin Huang

Joseph Bright

Guowen Meng

*See next page for additional authors*

Follow this and additional works at: [https://scholarworks.umass.edu/che\\_faculty\\_pubs](https://scholarworks.umass.edu/che_faculty_pubs)

---

---

**Authors**

Haibin Tang, Chih-Jung Chen, Zhulin Huang, Joseph Bright, Guowen Meng, Ru-Shi Liu, and Nianqiang Wu

---

# Plasmonic hot electrons for sensing, photodetection, and solar energy applications: A perspective F

Cite as: J. Chem. Phys. **152**, 220901 (2020); <https://doi.org/10.1063/5.0005334>

Submitted: 21 February 2020 . Accepted: 17 May 2020 . Published Online: 11 June 2020

Haibin Tang,  Chih-Jung Chen, Zhulin Huang, Joeseph Bright, Guowen Meng, Ru-Shi Liu, and  Nianqiang Wu

## COLLECTIONS

F This paper was selected as Featured



View Online



Export Citation



CrossMark

## ARTICLES YOU MAY BE INTERESTED IN

### Special topic on emerging directions in plasmonics

The Journal of Chemical Physics **153**, 010401 (2020); <https://doi.org/10.1063/5.0017914>

### Photoinduced phase separation in the lead halides is a polaronic effect

The Journal of Chemical Physics **152**, 230901 (2020); <https://doi.org/10.1063/1.5144291>

### Hot electron and thermal effects in plasmonic photocatalysis

Journal of Applied Physics **128**, 041101 (2020); <https://doi.org/10.1063/5.0013945>



New

## Your Qubits. Measured.

Meet the next generation of quantum analyzers

- Readout for up to 64 qubits
- Operation at up to 8.5 GHz, mixer-calibration-free
- Signal optimization with minimal latency

Find out more



# Plasmonic hot electrons for sensing, photodetection, and solar energy applications: A perspective

Cite as: J. Chem. Phys. 152, 220901 (2020); doi: 10.1063/5.0005334

Submitted: 21 February 2020 • Accepted: 17 May 2020 •

Published Online: 11 June 2020





View Online



Export Citation



CrossMark

Haibin Tang,<sup>1,2</sup> Chih-Jung Chen,<sup>3</sup>  Zhulin Huang,<sup>1</sup> Joeseeph Bright,<sup>2</sup> Guowen Meng,<sup>1</sup> Ru-Shi Liu,<sup>3,4,a)</sup> and Nianqiang Wu<sup>5,a)</sup> 

## AFFILIATIONS

<sup>1</sup>Key Laboratory of Materials Physics, and Anhui Key Laboratory of Nanomaterials and Nanotechnology, Institute of Solid State Physics, Chinese Academy of Sciences, Hefei, Anhui, 230031, People's Republic of China

<sup>2</sup>Department of Mechanical and Aerospace Engineering, West Virginia University, Morgantown, West Virginia 26506-6106, USA

<sup>3</sup>Department of Chemistry, National Taiwan University, Taipei 10617, Taiwan

<sup>4</sup>Department of Mechanical Engineering and Graduate Institute of Manufacturing Technology, National Taipei University of Technology, Taipei 10617, Taiwan

<sup>5</sup>Department of Chemical Engineering, University of Massachusetts Amherst, Amherst, Massachusetts 01003-9303, USA

<sup>a)</sup>Authors to whom correspondence should be addressed: [nianqiangwu@umass.edu](mailto:nianqiangwu@umass.edu) and [rsliu@ntu.edu.tw](mailto:rsliu@ntu.edu.tw)

## ABSTRACT

In plasmonic metals, surface plasmon resonance decays and generates hot electrons and hot holes through non-radiative Landau damping. These hot carriers are highly energetic, which can be modulated by the plasmonic material, size, shape, and surrounding dielectric medium. A plasmonic metal nanostructure, which can absorb incident light in an extended spectral range and transfer the absorbed light energy to adjacent molecules or semiconductors, functions as a “plasmonic photosensitizer.” This article deals with the generation, emission, transfer, and energetics of plasmonic hot carriers. It also describes the mechanisms of hot electron transfer from the plasmonic metal to the surface adsorbates or to the adjacent semiconductors. In addition, this article highlights the applications of plasmonic hot electrons in photodetectors, photocatalysts, photoelectrochemical cells, photovoltaics, biosensors, and chemical sensors. It discusses the applications and the design principles of plasmonic materials and devices.

Published under license by AIP Publishing. <https://doi.org/10.1063/5.0005334>

## I. INTRODUCTION

The term “hot carriers” defines the charge carriers (electrons and holes) in a non-equilibrium state with larger energy than in the thermal equilibrium state. Generally, high temperature, light (ultraviolet light, typically), and high electric fields excite or extract hot carriers. In contrast, surface plasmon resonance (SPR) is unique to excite hot carriers. In properly designed nanostructures of metals (typically Au, Ag, and Cu), free electrons will oscillate collectively if the incident light matches the resonant frequency of the collective electrons, known as SPR, including localized surface plasmon resonance (LSPR) and surface plasmon polaritons (SPPs). The

collective oscillation, which is called plasmon, dephases quickly, releasing the energy stored in the plasmon through (i) far-field light scattering (radiatively), (ii) near-field electromagnetic field enhancement (non-radiatively), (iii) hot carrier generation, and (iv) plasmonic heat effects. The branching ratio of these processes depends on the size, shape, and local media surrounding the plasmonic metal nanostructures. Each of these energy transfer processes can be used for a specific application. Some review articles have dealt with the plasmonic applications in enhanced light trapping from the far-field radiation effect,<sup>1,2</sup> surface-enhanced Raman scattering (SERS) or enhanced infrared absorption from the near-field enhancement effect,<sup>3,4</sup> water steam generation (seawater desalination),



cancer therapy from plasmonic heat effect,<sup>5–7</sup> photodetection,<sup>8</sup> photovoltaics,<sup>9</sup> photocatalysis, and photochemistry.<sup>10–13</sup> This review article attempts to present the perspective and the correlations of three application fields of plasmonic hot electrons—sensing, photodetection, and solar energy conversion.

This review article deals with plasmonic hot carriers, which are generated in plasmonic metal nanostructures under illumination of visible- or infrared-light.<sup>14,15</sup> Both hot electrons and hot holes are involved in interesting physical or chemical processes. Since holes are paired with electrons and hot electrons are much easier to measure than hot holes, previous research was predominantly focused on hot electrons, while there are a few reports on hot holes. However, hot holes are attracting increasing interest in research.<sup>16–18</sup> This review is focused on the applications of plasmonic hot electrons in sensing, photodetection, and solar energy conversion. The general design principle for each application is summarized and explained with a few typical examples. In order to better understand the applications, the processes of plasmonic hot electron generation, decay, and transfer are presented briefly. The analytical techniques for characterization of plasmonic hot electrons are introduced herein. In particular, plasmonic hot electrons are abundant and have high energy levels but short-lived. These unique features bring new opportunities to applications, accompanied by new challenges.

## II. GENERATION AND EXTRACTION OF PLASMONIC HOT CARRIERS

### A. Generation and timescale of hot carriers in metallic nanostructures

For an isolated metal nanostructure under light illumination, excitation of SPR results in light collection from an area much larger than its geometrical cross-sectional area [Fig. 1(a)].<sup>19</sup> Subsequently, the plasmon (coherent electron oscillations) can dephase non-radiatively through Landau damping, generating hot electron-hole pairs at the timescale of 1–100 fs [Fig. 1(b)].<sup>20,21</sup> The electrons from the occupied energy levels are excited above the Fermi energy, reaching the energetic level of  $E_F + \hbar\omega_{\text{LSPR}}$ , where  $E_F$  and  $\hbar\omega_{\text{LSPR}}$  refer to the Fermi level and LSPR energy, respectively. These high energetic hot electrons will quickly transfer their energy to the thermal equilibrium electrons, which leads to the deviation from the equilibrium level and the in-turn effect on hot electrons. Meanwhile, the generated hot electrons redistribute their energy to the lower-energy electrons.<sup>22,23</sup> In other words, multiplication of hot electrons takes place via the electron–electron scattering processes, resulting in the energy loss of partial hot electrons.<sup>24</sup> The percentage and population of hot carriers among the whole charge carriers depend on the electronic structure of metal nanostructures and incident photon energy.<sup>25,26</sup> At the timescale of 100 fs to 1 ps, hot carriers are

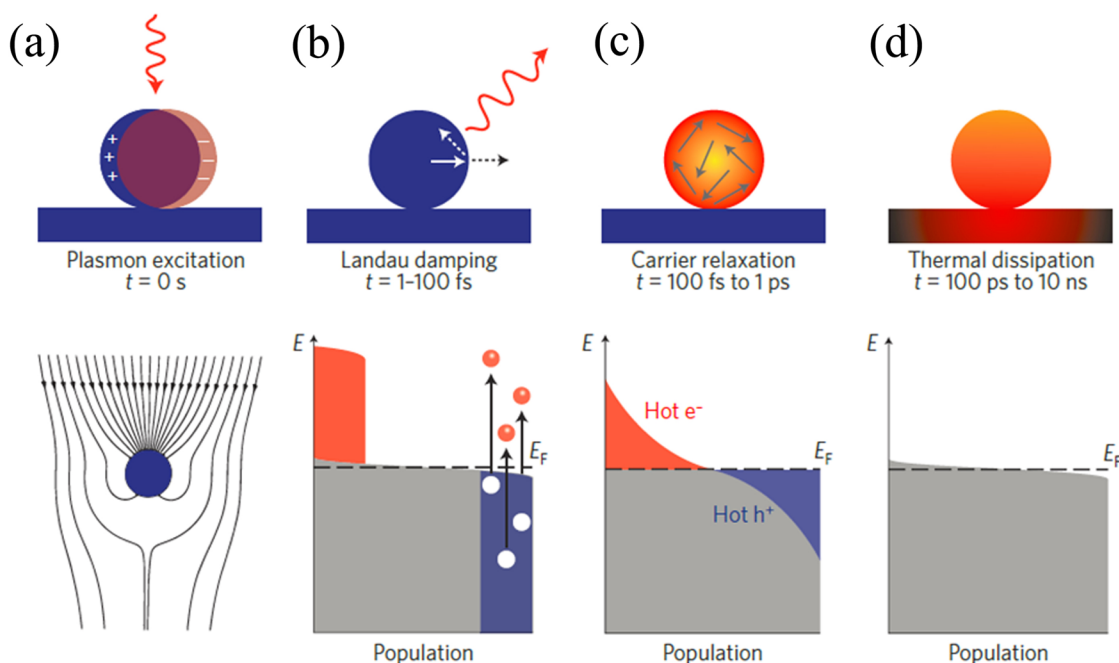


**FIG. 1.** Excitation and dephasing of a plasmon in metal nanoparticles. (a) Excitation of a localized surface plasmon enhances light absorption. (b) Generation and multiplication of hot carriers in 1–100 fs through Landau damping. (c) Hot carriers redistribute their energy into the Fermi–Dirac-like distribution at the timescale of 100 fs to 1 ps due to the electron–electron interaction. (d) Heat is released to the surroundings via thermal conduction in 100 ps to 10 ns. Note that the gray area represents the population of the electronic states; hot electrons and hot holes are represented by the red and blue area, respectively. Reproduced with permission from Brongersma *et al.*, *Nat. Nanotechnol.* **10**, 25 (2015). Copyright 2015, Macmillan Publishers Limited.

finally thermalized to a Fermi–Dirac-like distribution [Fig. 1(c)].<sup>27,28</sup> With a change in the velocity of partial electrons due to the electron–electron interaction, the interactions with phonons increase. The interaction between the hot electrons and phonons continues over a longer timescale of several picoseconds, which will result in a quasi-equilibrium state between the electron system and the phonon system, elevating the lattice temperature.<sup>13,28</sup> Finally, heat is transferred to the surroundings of the metal structure at the timescale of 100 ps to 10 ns [Fig. 1(d)].

## B. Hot electron transfer

When adsorbate molecules or semiconductors are directly attached to a metal nanostructure, hot electrons can be captured and extracted to the adsorbates or semiconductors before thermalization into heat. This provides a new photoconversion route for photochemistry, photovoltaics, photodetection, and sensing.<sup>10,29,30</sup> In general, there are two pathways for hot electron transfer, indirect transfer and direct transfer.<sup>10,31</sup> In the indirect transfer process,<sup>32,33</sup> hot electrons are first generated in the plasmonic metal, and some of them transfer to either the adsorbate or the semiconductor. Owing to rapid relaxation via electron–electron scattering, only a very small fraction of plasmonic hot electrons with high potential energy, which are able to overcome the energy barrier at the interface, can be involved into the indirect transfer process. The hot electron injection process is competing with the electron–electron scattering process. This is one of the reasons that the indirect transfer process exhibits a very low efficiency (typically <2%). Another reason is that the back transfer of electrons may take place at the interface, especially in the case of a low energy barrier height. For the direct hot-electron transfer process,<sup>34–36</sup> the presence of suitable empty hybridized orbitals resulting from the strong interaction of the metal with the adsorbate molecules or closely contacted semiconductors facilitates the direct generation of hot electrons in the empty hybridized orbitals

during dephasing of plasmon. Compared to the indirect electron transfer, the direct transfer process has higher transfer efficiency and lower energy loss. This is because the indirect transfer pathway suffers from a lot of energy loss in the electron–electron and electron–phonon scattering before transferring and in the hot electron injection across the heterojunction interface. However, in the direct electron transfer pathway, hot electrons are directly generated in the hybridized orbitals due to Landau damping, which avoids the electron–electron scattering in the metal and energy loss during the injection process across the interface. After injection, hot electrons will interact with the semiconductor or adsorbates and/or back transfer to the metal, which competes with the hot electron transfer processes, creating a barrier for an efficient utilization of plasmonic hot electrons.

### 1. Metal–adsorbate complexes

Calculation and experiments reveal that two significant Raman peaks of *p*-aminothiophenol (*p*-ATP) on the nanostructured Au or Ag substrates appeared under laser excitation, which was due to the formation of a new chemical species, *p,p'*-dimercaptoazobenzene (DMAB), by coupling of adjacent *p*-ATP molecules.<sup>29,37–39</sup> This gave direct evidence of hot electron-induced chemical transformation on plasmonic metal nanoparticles (NPs).

The two-step indirect transfer is considered to be one of the pathways for the hot electron-driven chemical reaction [Fig. 2(a)]. It assumes that hot electrons are first generated within metal nanoparticles resulting from Landau damping. Subsequently, hot electrons with suitable energy can transfer into the lowest unoccupied molecular orbitals (LUMOs) of adsorbates across the interfacial barrier, followed by the thermalization process (interaction with the adsorbates).<sup>40,41</sup> In this case, the hot electron transfer efficiency is dependent on the incident photon energy, the interface of the metal/adsorbate molecules, the density of states of the metal

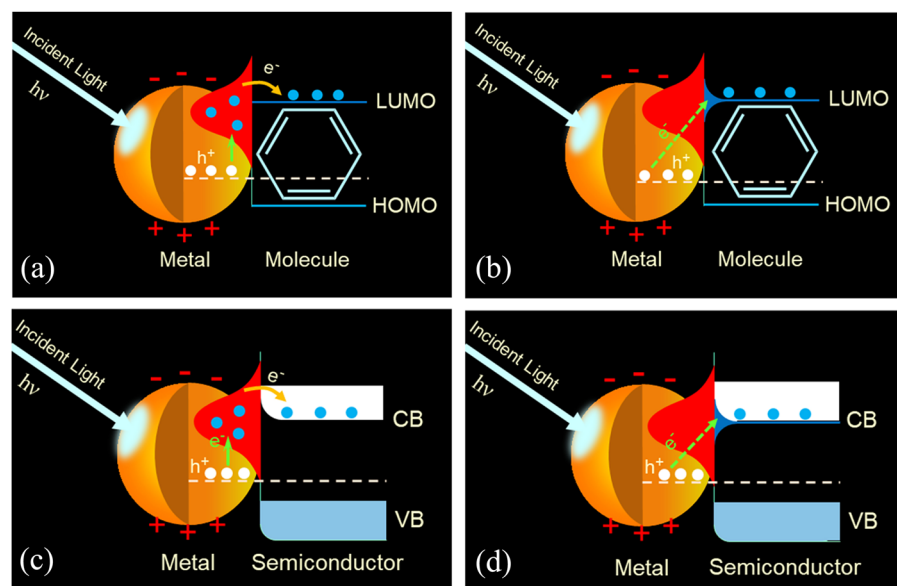


**FIG. 2.** Plasmonic hot electron transfer pathways from a metal to an adsorbate or a semiconductor. (a) Indirect and (b) direct transfer from a metal to an adsorbate. (c) Indirect and (d) direct transfer from a metal to a semiconductor. Adapted with permission from N. Wu, *Nanoscale* **10**, 2679 (2018). Copyright 2018, The Royal Society of Chemistry.

nanostructures, and the energy of the LUMO (i.e., the plasmonic energetic level is higher than the LUMO of adsorbates). Since hot electrons are excited in the metal and then transferred out, the optimum efficiency for hot electron transfer occurs when the incident wavelength matches the peak wavelength of the SPR of metal nanostructures.

Recently, theory and experiments revealed that the timescale for hot electron generation and transfer from the metal to adsorbed molecules was, in some cases, much shorter than that expected with the indirect transfer mechanism (Fig. 3).<sup>34–36</sup> This has aroused an interest in the direct electron transfer pathway originating from the chemical interface damping (CID) [Fig. 2(b)]. The strong interaction of the metal and the adsorbates results in orbital hybridization. With the suitable orbital overlap, the plasmon excited by light illumination will directly dephase, generating hot electrons in the empty hybridized orbitals on the adsorbate side. Because there are neither electron–electron scattering nor energy losses due to interface injection, the theoretical maximum efficiency is much higher than that of the indirect transfer process. The optimum efficiency is achieved when the light wavelength meets two conditions simultaneously: (i) the incident light wavelength can excite the SPR and (ii) the energetic level of the SPR is powerful enough to induce the HOMO–LUMO transition of the hybridized surface states.<sup>42</sup>

In this case, compared to the conventional electron–electron scattering and electron–phonon scattering in metals, a new thermalization pathway is revealed in the metal/adsorbate hybrid system known as chemical interface scattering (CIS).<sup>43–45</sup> Hot electrons transiently transfer into the adsorbates and transfer back into the metal, leaving a portion of energy in the adsorbates. This process occurs repeatedly, resulting in accumulation of energy within the adsorbates and activating the adsorbates. Such a cycling process can effectively extend the lifetime of hot electrons ( $\sim 10$  ps), as shown in Fig. 3. This is obviously beneficial to photochemical reactions.

## 2. Metal-semiconductor heterojunctions

A plasmonic metal was used for enhancing the photoelectrochemical activity in the 1990s.<sup>46,47</sup> The direct evidence of plasmonic hot electron injection to a semiconductor was demonstrated in the 2000s.<sup>32,33,48,49</sup> There are also two different routes for the hot electron transfer in the metal/semiconductor system. As shown in Fig. 2(c), hot carriers are first generated in the metal through plasmonic dephasing, and then the hot electrons with sufficient energy

can overcome the Schottky barriers at the metal/semiconductor and enter the conduction band (CB) of the semiconductor. Recent studies have revealed that the hot electron injection is strongly dependent on the LSPR energy with respect to the Schottky barrier height.<sup>50–54</sup> The plasmonic hot electron injection occurs only when the LSPR energy is sufficient for overcoming the Schottky barrier. If the Schottky barrier is too high, only a small portion of hot electrons have sufficient energy to overcome it. However, if the Schottky barrier is too low or absent, the hot electrons, which had been injected into the semiconductor CB, will quickly transfer back to the metal.<sup>11</sup> In addition, the electron transfer efficiency is dependent on the quality of interface (i.e., defects, the interaction between the metal and semiconductor) and the incident light energy. The maximum theoretical efficiency for an indirect hot-electron transfer to a semiconductor is calculated as 8%.<sup>41,55</sup> However, the experiment-realized efficiency is much lower than this, typically  $< 2\%$ .<sup>30,56–62</sup>

The hot electron transfer timescale for an Au/TiO<sub>2</sub> heterostructure was demonstrated to be less than 50 fs by transient absorption spectroscopy.<sup>50–54</sup> This was much faster than that expected in the indirect transfer mechanism (Fig. 3). Based on the timescale and energy transfer efficiency, a direct transfer mechanism was proposed and confirmed experimentally,<sup>63,64</sup> which was analogous to the CID process in the metal/adsorbate case. In this model, the plasmonic dephasing in metal/semiconductor heterostructures directly excites electrons to the empty hybridized states, which are centered in the semiconductor with holes left in the occupied hybridized states, which are centered in the metal [Fig. 2(d)].

## C. Energetic distribution of hot carriers

The energy distribution of plasmonic hot carriers is narrow-band and strongly dependent on the metal, particle size, geometry, medium, and carrier lifetime.<sup>20,25,26,41,65–70</sup> Since the lifetime of hot carriers is very short, these dependences are revealed by theoretical simulation originally. There is a strong reason to develop accurate experimental techniques with high time resolution.

Small plasmonic nanoparticles are more efficient for hot carrier generation than the larger nanoparticles. Nordlander *et al.* calculated the energy distribution of hot carriers in Ag nanoparticles (NPs).<sup>26</sup> The results revealed that larger Ag NPs had a higher production rate of hot carriers but with a lower carrier energy [Fig. 4(a)]. Meanwhile, the lifetime of hot carriers also strongly affects the

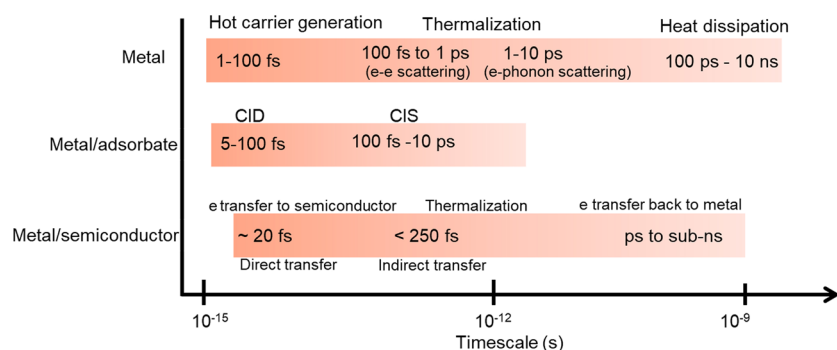


**FIG. 3.** Timescales of different plasmonic hot carrier injection cases. Note that e stands for the electron. Adapted with permission from Zhang *et al.* Chem. Rev. **118**, 2927 (2018). Copyright 2017, American Chemical Society.

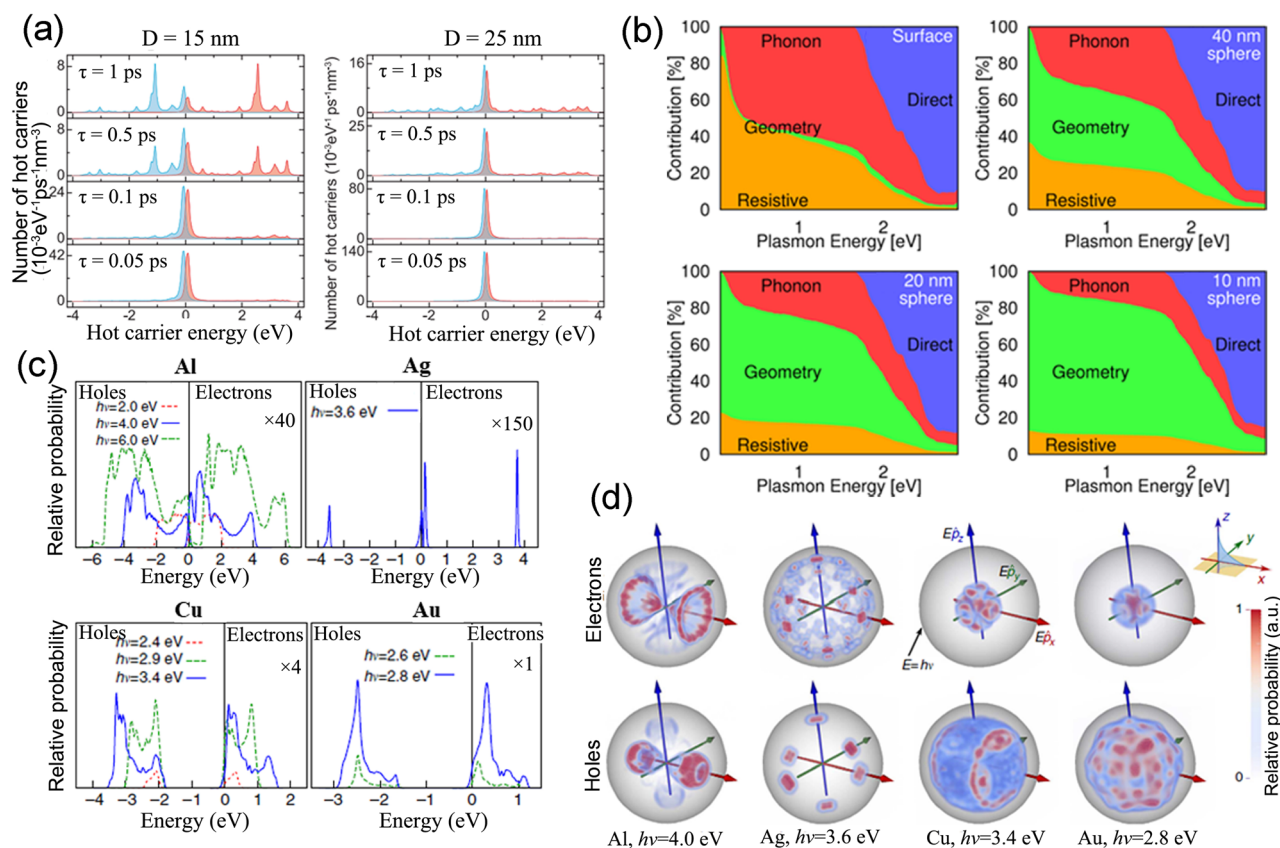


**FIG. 4.** Factors governing hot carrier energetic distribution. (a) The distribution of hot electrons (red) and hot holes (blue) with different lifetimes ranging from 0.05 ps to 1 ps in Ag nanoparticles of 15 nm and 25 nm. Adapted with permission from Manjavacas *et al.*, ACS Nano 8, 7630 (2014). Copyright 2014, American Chemical Society. (b) Comparison of influences of resistive, geometry-assisted, phonon-assisted, and direct-transition on the absorption for Au spheres of 40 nm, 20 nm, or 10 nm in diameter and films. Adapted with permission from Brown *et al.*, ACS Nano 10, 957 (2016). Copyright 2016, American Chemical Society. (c) Hot carrier energy and (d) momentum-direction distributions for Al, Ag, Cu, and Au. Adapted with permission from Sundararaman *et al.*, Nat. Commun. 5, 5788 (2014). Copyright 2014; licensed under a Creative Commons Attribution (CC BY) license.

energy distribution of hot carriers. For longer lifetimes, plasmon decay results in highly energetic hot carriers, whereas for shorter carrier lifetimes, the energy is closer to the Fermi energy of the metal (very low energy). The geometry, including the shape and aspect ratio, also significantly affects the generation and ejection of hot carriers due to carrier confinement and surface scattering effects.<sup>68,71</sup> The same conclusion was demonstrated by Brown *et al.*,<sup>65</sup> showing the influence of phonon, geometry, and classic resistive effects with the Au nanoparticles [Fig. 4(b)]. Obviously, the energy distribution of hot carriers is highly dependent on the size of plasmonic nanoparticles. Different plasmonic metals with different electronic band structures have a diverse energy distribution. Atwater *et al.* revealed that Au and Cu produced holes with a higher energy of 1–2 eV than electrons, while Ag and Al have equal energy for both electrons and holes [Fig. 4(c)].<sup>69,70</sup> They also found the momentum-direction distributions for hot carriers that were anisotropic [Fig. 4(d)].

It is important to understand the energetic distribution of hot carriers in the plasmonic metal itself. It is also essential to clarify

the energetic distribution of hot carriers after they are transferred from the plasmonic metal to the surface adsorbates or to the adjacent semiconductors. In conventional organic dye- or quantum dot-sensitized semiconductors, the electrons are quickly thermalized to the conduction band edge of the semiconductor after the photo-excited electrons are transferred from the organic dye (or quantum dot) to the semiconductor. That is, the transferred electrons exhibit a thermal distribution in energetics. In contrast, in plasmonic metal–semiconductor heterojunctions, the transferred electrons in the semiconductor show a non-thermalized distribution in energetics after plasmonic hot electrons are injected from the metal to the conduction band of the semiconductor if the semiconductor layer is thin.<sup>72</sup> That is, the plasmonic hot electrons transferred to the semiconductor are still “hot.” This indicates that the plasmon-sensitized semiconductor could show a higher open voltage for photovoltaics and a larger thermodynamic driving force for photocatalytic reactions, as compared to the conventional organic dye- or quantum dot-sensitized semiconductors. The non-thermalized distribution of the transferred hot electrons in the



semiconductor can be tuned by the shape of the plasmonic metal nanostructure.<sup>72</sup> Among three types of Au@TiO<sub>2</sub> core-shell nanoparticles with nanospheres, nanorods, and nanostars as the cores, more hot electrons are distributed at relatively high energetic levels for Au nanostar@TiO<sub>2</sub> and Au nanorod@TiO<sub>2</sub>.

#### D. Analytical tools for hot carrier characterization

It is important to experimentally track the excitation and dephase of plasmon in a time-resolved manner. However, the excitation and collective behaviors of plasmon under a pulsed light excitation are extremely fast (typically less than 10 fs), which made it almost impossible to be measured with the state-of-the-art analytical techniques. Current transient absorption spectroscopy (TAS) generally exhibits a time resolution of ~30 fs, which enables tracking the late-stage dephase of plasmon and the hot electron transfer from the metal to the semiconductor (or adsorbate). In addition, x-ray absorption near edge structure (XANES) provides an effective tool for measuring the energetic level of plasmonic hot electrons. Currently, TAS and XANES are two major analytical tools for characterization of plasmonic hot electrons.

#### 1. X-ray absorption near edge structure (XANES) spectroscopy

X-ray absorption spectroscopy (XAS) is a powerful analytic tool for characterizing the electronic, structural, and magnetic properties of materials with not only high crystallinities but also short-term ordered or even amorphous structures. XANES utilizes synchrotron x-ray radiation as the excitation source, exhibiting high intensity, continuous spectrum, excellent collimation, and tiny probe size. The core electrons are excited to the unoccupied electronic states within

the analyte. As such, the absorption edge corresponds to the binding energy of a core-level state that is characteristic of the energetics and chemical shift.

The CB of various semiconductor materials is composed of different orbitals. For instance, the CB of wurtzite ZnO mainly comprises the Zn 4s and 4p states.<sup>73</sup> The CB of rutile TiO<sub>2</sub> is dominant by the Ti 3d orbitals.<sup>74</sup> The absorption edges in XANES spectra can be used to investigate the electronic transition from the core levels to the CB of semiconductors. The Ti L-edge absorption can be used to resolve the CB of TiO<sub>2</sub> since the excitation involves the 2p and 3d orbitals. In contrast, the details of CB in ZnO can be revealed by the Zn K-edge absorption, which is attributed to the electronic transition from the 1s to 4p states. Moreover, the XANES intensity is related to the electron occupancy of CB in the semiconductors. Thus, the population of hot electron injection to the semiconductor from the plasmonic metal can be characterized by XANES, as illustrated in Fig. 5(a).

Amidani *et al.* prepared pure and N-doped TiO<sub>2</sub>, which were decorated with Au-NPs with an LSPR band at ~550 nm.<sup>75</sup> The pre-edge region of Ti K-edge absorption spectra of the TiO<sub>2</sub>/Au and N-TiO<sub>2</sub>/Au powder obtained under irradiation of a 532 nm laser was different from those in the dark. Pure TiO<sub>2</sub> cannot be excited by the 532 nm laser due to a large bandgap, while N-TiO<sub>2</sub> was able to be slightly excited by a 532 nm laser because its band structure was altered by N doping. However, the shape and amplitude of the laser on/off spectral differences for TiO<sub>2</sub>/Au and N-TiO<sub>2</sub>/Au powders were analogous. The change in the Ti K-edge absorption spectrum induced by the 532 nm laser did not result from the plasmon-induced resonance energy transfer (PIRET), which would be energetically allowed only for N-TiO<sub>2</sub>/Au, but not for TiO<sub>2</sub>/Au. Hence, hot electron injection from the Au-NPs to the CB of TiO<sub>2</sub>

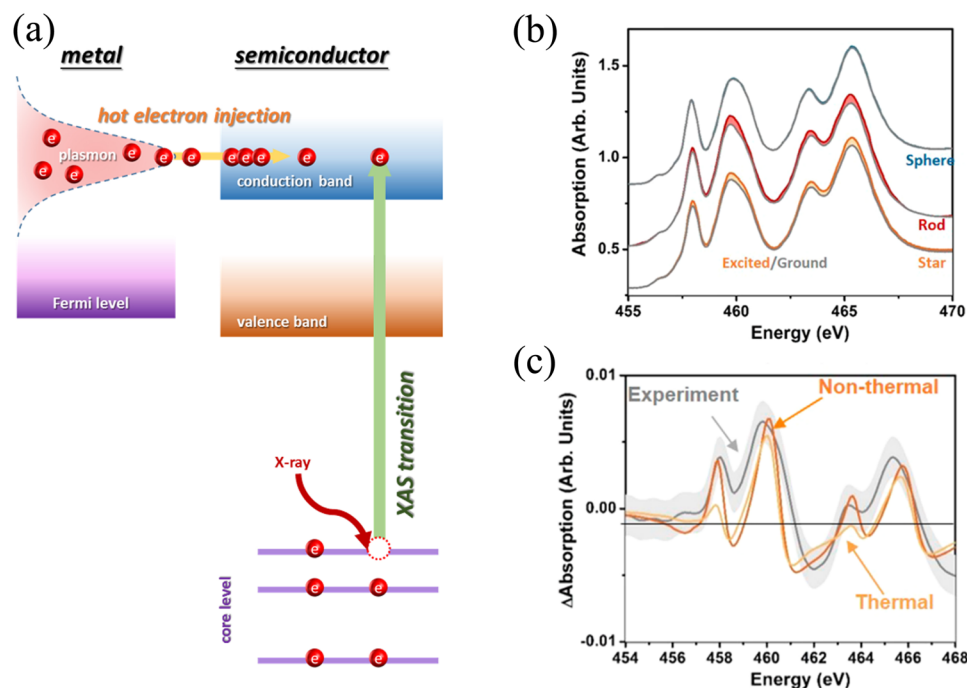


**FIG. 5.** (a) Schematic illustration of XANES measurements of plasmonic hot carriers. The injection of plasmonic hot electrons alters the CB state density of the semiconductor, altering the amplitude of the absorption edge. (b) Ti L-edge XANES spectra for the Au@TiO<sub>2</sub> core-shell nanoparticles in the dark and under visible-light illumination (plasmonic excitation). (c) The differential absorption of Ti L-edge XANES spectra for Au nanostar@TiO<sub>2</sub>, combined with the theoretical predictions. Adapted with permission from Cushing *et al.*, ACS Nano 12, 7117 (2018). Copyright 2018, American Chemical Society.

was believed to cause its electronic transition difference. Therefore, Hung *et al.* investigated the plasmonic effect on the CB of TiO<sub>2</sub> nanorods (TiNR) using the Ti L-edge XANES spectra since the electrons in the 2p orbitals are excited to the 3d states.<sup>74</sup> As compared to the dark condition of TiNR–Au, a positive variation was shown under visible light irradiation. Electromagnetic fields of plasmonic Au significantly induced the vacancies in the CB of TiNR and enhanced the possibility of Ti L-edge excitation. However, further modifying IrO<sub>x</sub> on the Au surface provided a considerably opposite behavior, as compared with TiNR–Au. The Ti L-edge peak intensity of TiNR–Au–IrO<sub>x</sub> was reduced under visible light irradiation. This observation suggests that the hot holes rapidly transferred from Au to IrO<sub>x</sub> by accelerating the kinetics of hot holes, improving the separation of hot carriers. The increased amount of hot electrons injected into the CB of TiNR resulted in a decrease in the Ti L-edge excitation intensity. By modifying IrO<sub>x</sub> on the Au surface, the recombination of hot carriers was suppressed, leading to a hot electron injection-dominated CB nature of TiNR rather than a plasmon-induced electromagnetic field variation. Recently, XANES measurement was performed to study the energetics of the hot electrons in TiO<sub>2</sub> injected from Au in the Au@TiO<sub>2</sub> core-shell nanoparticles [Fig. 5(b)].<sup>72</sup> The experimental results combined with the theoretical predictions show that plasmonic hot electrons exhibited a non-thermalized distribution in TiO<sub>2</sub> after they transferred to TiO<sub>2</sub> from Au, as shown in Fig. 5(c). Furthermore, the energetic distribution of the injected hot electron in TiO<sub>2</sub> was dependent on the shape of the Au core.

## 2. Transient absorption spectroscopy (TAS)

Understanding the kinetics of the generation and transfer of plasmonic hot carriers is very important in designing plasmonic materials and devices. The generation of plasmonic hot carriers and energy relaxation through electron–electron and electron–phonon scattering in metals all occur on a timescale of several femtoseconds to picoseconds.<sup>76</sup> Additionally, the plasmonic hot electron injection from the metals into the neighboring semiconductors or adsorbates is also very fast, typically at the sub-picosecond timescale. Ultra-fast time-resolved pump–probe measurements, such as transient absorption spectroscopy (TAS), can be used to analyze the

lifetime or kinetics of hot carriers in plasmonic materials.<sup>50,52</sup> In TAS [Fig. 6(a)], electrons of the sample are promoted to an excited state via a pump pulse. A second pulse with a weaker intensity (white or monochromatic light), functioned as a probe, penetrates through the analyte with a time delay ( $\tau_1$ ), as compared with the pump pulse. The absorption difference between the ground and excited states of the analyte will occur because of a change in the carrier population resulting from the excitation or the transfer of hot electron. This absorption difference is recorded with the various time delays ( $\tau_2, \tau_3, \dots$ ) in which one can track the charge carrier evolution with the time [Fig. 6(b)]. Additionally, if one collects the absorption under the same delay time but using the probe pulse with a continually varied wavelength, a spectrum of absorption (charge carrier population) with the wavelength can be obtained, which also provides information on the kinetic process at the timescale of femtosecond.<sup>77,78</sup>

As mentioned above, the plasmon is dephased through radiative decay (photon emission) or/and non-radiative decay (Landau damping). Plasmonic hot electrons are generated by Landau damping (<100 fs). The generated hot electrons with a non-thermal distribution are relaxed to the Fermi electron distribution through several steps (Figs. 1 and 3):<sup>13,28,77</sup> (i) electron–electron scattering during Landau damping (<100 fs), (ii) continued electron–electron scattering (100 fs–1 ps and transformation of the non-thermal distribution to the thermal distribution), (iii) electron–phonon scattering (1–10 ps, transfer of energy from electrons to the lattice, and cooling of hot electrons), and (iv) phonon–phonon interaction (~100 ps–10 ns and heat dissipation through the lattice).

The timescale of electron–electron scattering relaxation for small metal nanoparticles is estimated to be ~200 fs,<sup>21</sup> leading to the transformation of the non-thermal distribution to the thermal (Fermi–Dirac) distribution. In the thermal distribution, only a small portion of electrons are on the high energetic level. Therefore, it is better to finish the hot electron transfer from a metal to a semiconductor before relaxation to the thermal distribution (Fig. 3). A recent study shows that the hot electron injection process in the Au–TiO<sub>2</sub> heterojunction becomes inefficient after electron–electron scattering relaxation (at the timescale of ~100 fs).<sup>50</sup> Furube and co-workers utilized the visible-pump/infrared-probe TAS for resolving

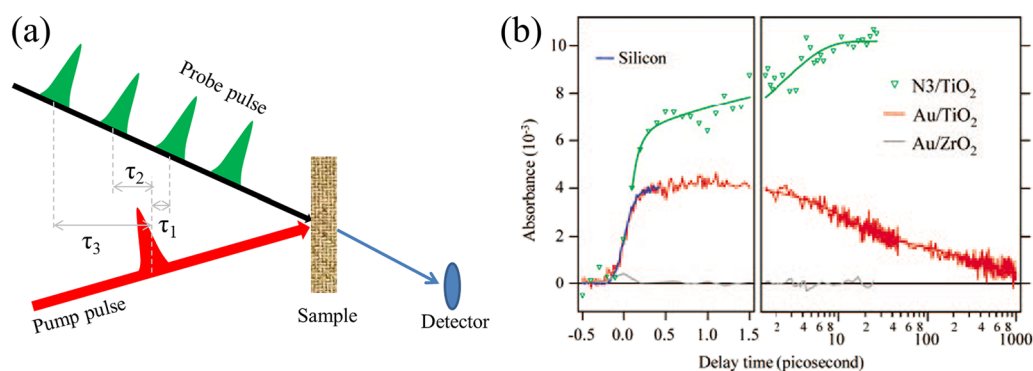


**FIG. 6.** (a) Schematic illustration of the transient absorption spectroscopy principle. (b) Transient absorption kinetics in a hybrid structure of dye-sensitized TiO<sub>2</sub> (N3/TiO<sub>2</sub>), Au/ZrO<sub>2</sub>, and Au/TiO<sub>2</sub>. Adapted with permission from Furube *et al.*, *J. Am. Chem. Soc.* **129**, 14852 (2007). Copyright 2007, American Chemical Society.

the lifetime of charge transfer between Au and TiO<sub>2</sub>.<sup>50</sup> Their results indicated that the hot electron injection occurred within 220 fs. After the indirect transfer in a metal–semiconductor heterojunction, both the non-thermal distribution and the thermal distribution are possible for the injected electrons in the semiconductor, and non-thermal distribution can be dominant in many cases.<sup>72</sup> On the other hand, the lifetime of plasmonic hot electrons in the metal alone is very short. However, after hot electrons are transferred into a semiconductor, their lifetime could be extended due to the reduced electron–electron and electron–phonon scattering. Naldoni *et al.* revealed that the sites of Au-NPs on TiO<sub>2</sub> brookite nanorods had a significant influence on the decay time by TAS.<sup>53</sup> In the case of Au-NPs distributed throughout the thickness of the TiO<sub>2</sub> thin film, the hot carrier lifetimes were found to be on the order of a few hundreds of femtoseconds. The short lifetime was because the Au-NPs served as the recombination centers for excited carriers. However, in the case of Au-NPs decorated on the top surface of the TiO<sub>2</sub> thin film, the lifetime of hot electrons was 4 orders of magnitude longer due to efficient hopping on brookite lateral facets.

### III. APPLICATIONS OF PLASMONIC HOT CARRIERS

#### A. Sensing

Plasmonic hot electrons can bring new effects on physicochemical processes, such as physisorption or chemisorption of chemicals, selective oxidation, and direct reduction of adsorbates. The interaction can occur directly between a metal and the adsorbed

molecules or between a metal and an adjacent semiconductor. The interactions may result in (i) transformation of adsorbates, (ii) fluctuation of hot electron-induced current or conductivity, and (iii) modification of the SPR-related optical properties (transmittance and adsorption). By transducing these interactions, various sensors can be designed based on plasmonic hot electrons accordingly. The plasmon-mediated chemical transformation has been well-demonstrated. Transformation of chemical species could change the dielectric environment of the plasmonic nanostructures, modulating the SPR-related optical properties. This, in turn, affects the generation of plasmonic hot electrons. Thus, photoelectric sensors can be designed.

#### 1. Gas sensors

Generally, resistive gas sensors are designed based on the Schottky junctions in which the resistivity can be modulated either by the Schottky barrier or by the electron flow across the Schottky barrier.<sup>79–84</sup> Taking a hydrogen sensor as an example, Nienhaus *et al.* devised a metal–semiconductor Schottky diode for hydrogen detection.<sup>79</sup> They fabricated an ultrathin silver film (5 nm thick) that was comparable in thickness to the mean free path of hot electrons in *n*-Si(111), which was used for the selective detection of atomic hydrogen [Fig. 7(a)]. The hydrogen atoms impinged on the Ag film and underwent exothermic adsorption, creating hot electrons. The generated hot electrons then traveled ballistically through the Ag film and traversed the Schottky barrier into *n*-Si(111). Hot electrons were thus detected as a photocurrent, which was proportional to the

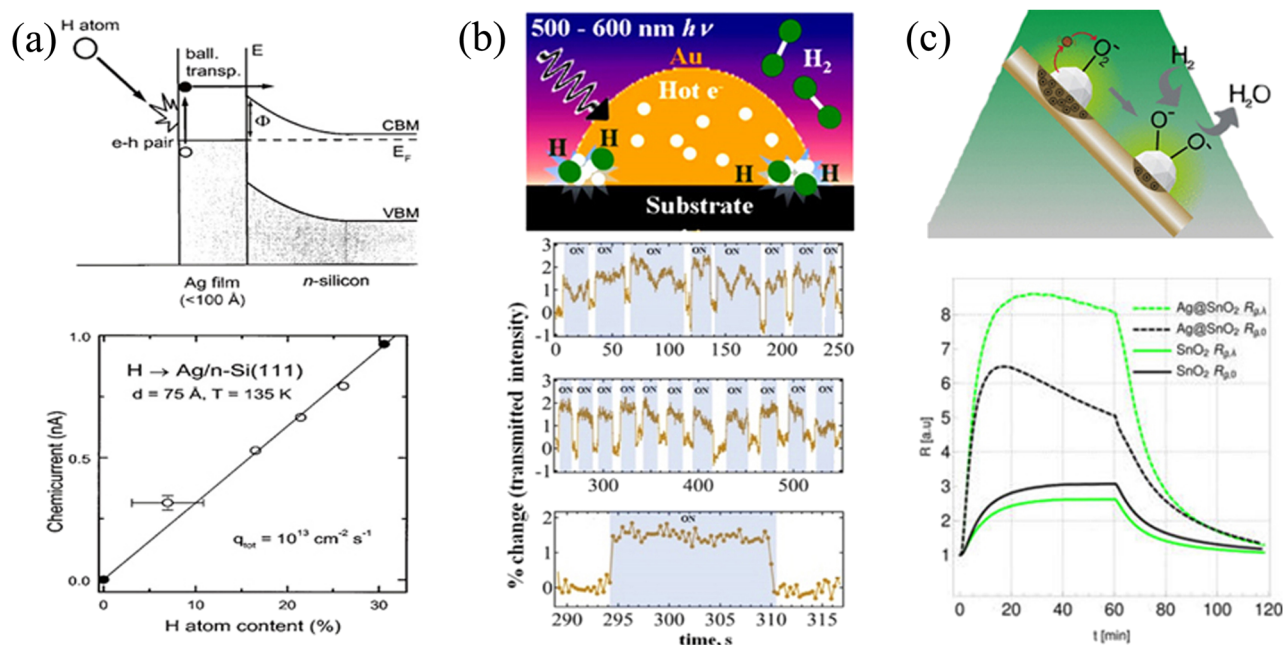


**FIG. 7.** Hydrogen sensors based on plasmonic hot electrons. (a) A H-atom detector based on generating *e*-*h* pairs. Photocurrent is proportional to the rate of hydrogen adsorption. Adapted with permission from Nienhaus *et al.*, Appl. Phys. Lett. **74**, 4046 (1999). Copyright 1999 AIP Publishing LLC. (b) A H<sub>2</sub> detector based on the change in transmission intensity. Adapted with permission from Sil *et al.*, ACS Nano **8**, 7755 (2014). Copyright 2014, American Chemistry Society. (c) A H<sub>2</sub> detector based on the change in conductivity. Adapted with permission from Cattabiani *et al.*, J. Phys. Chem. C **122**, 5026 (2018). Copyright 2018, American Chemical Society.

hydrogen adsorption rate. The theoretical limit of detection (LOD) for such a sensor was down to  $2 \times 10^{10}$  H atoms  $\text{cm}^{-2} \text{s}^{-1}$ , depending on the noise level ( $\sim 4$  pA). This protocol was further utilized for the detection of hot electron flow with the Pt-loaded Au/TiO<sub>2</sub> Schottky diodes during oxidation of CO and hydrogen.<sup>80,81</sup>

Halas group also reported that the plasmonic hot electrons could be transferred from Au-NPs into a Feshbach resonance of an H<sub>2</sub> molecule adsorbed on the Au surface, leading to dissociation of H<sub>2</sub> molecules under visible-light excitation at room temperature.<sup>85</sup> Following this mechanism, a plasmonic optical hydrogen sensor has been developed.<sup>86,87</sup> The hot electrons made the dissociated hydrogen atoms adsorb and diffuse into the thermally dewetted Au nanohemispheres, leading to the formation of a metastable Au hydride (AuH<sub>x</sub>) with a different dielectric constant from Au [Fig. 7(b)].<sup>86</sup> The change in the dielectric constant shifted the LSPR position of the particles and induced a

$\sim 1\%$ – $2\%$  change in optical transmission of the thin film. Cattabiani *et al.* demonstrated a conductometric H<sub>2</sub> sensor at room temperature using the Ag-NPs-decorated SnO<sub>2</sub> nanowires [Fig. 7(c)].<sup>87</sup> The plasmonic hot electrons from the Ag-NPs promoted the conversion of the adsorbed O<sub>2</sub><sup>-</sup> into highly reactive O<sup>-</sup>, which enhanced the catalytic dissociation of H<sub>2</sub>, leading to an increment in current.

Similarly, plasmonic hot electrons have been harnessed to dissociate the adsorbed gaseous molecules for the detection of other gaseous adsorbates, such as ammonia and acetylene. By utilizing an Au@ZnO-loaded porous silicon film, the photocurrent responded to a change in the ammonia concentration (down to 50 ppm) at room temperature.<sup>88</sup> Moreover, the Au-decorated ZnO nanowires as a transducer exhibited a concentration-dependent and time-dependent p–n transition response for the detection of C<sub>2</sub>H<sub>2</sub> gas at room temperature.<sup>83</sup>

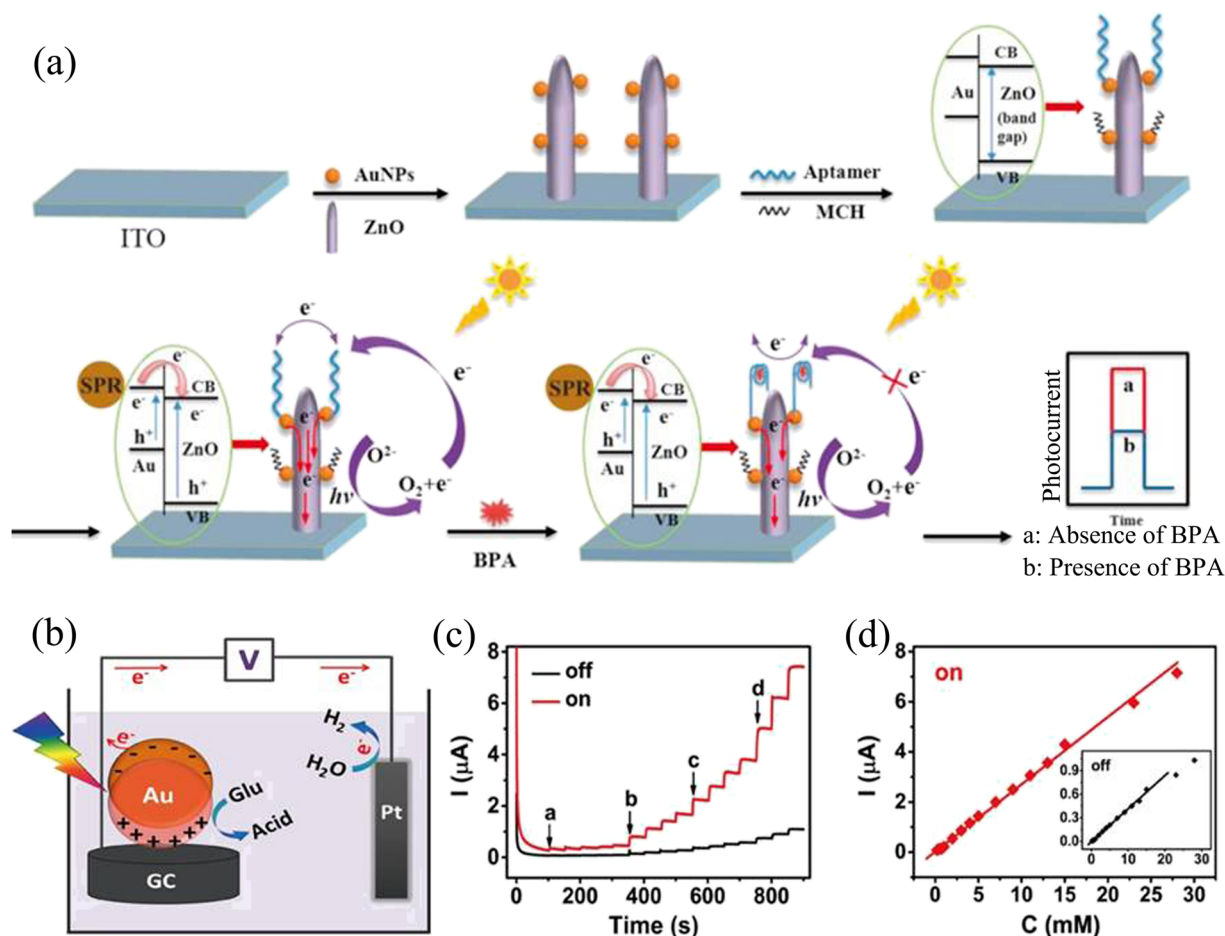


**FIG. 8.** Biosensors based on plasmonic hot electrons. (a) A photoelectrochemical aptasensor based on Au/ZnO nano-pencils for BPA detection. The Au/ZnO hybrid structures were deposited on ITO first. The Au/ZnO/ITO electrode was then functionalized with the aptamer and 6-mercapto-1-hexanol (MCH). The photocurrent was enhanced due to the plasmonic hot electron injection to ZnO from Au nanoparticles. Once BPA analytes were immobilized onto the photoanode, the photocurrent decreased due to the blockage of electron transfer. Adapted with permission from Qiao *et al.*, *Biosens. Bioelectron.* **86**, 315 (2016). Copyright 2016, Elsevier. (b) An electrochemical setup of the plasmon-enhanced glucose sensor. (c) The  $I$ - $t$  curves for glucose oxidation in 0.1M NaOH on the AuNPs/GC electrode at 0.3 V (vs Ag/AgCl). (d) A plot of the glucose sensor with and without LSPR excitation. Adapted with permission from Wang *et al.*, *ACS Nano* **11**, 5897 (2017). Copyright 2017, American Chemistry Society.



## 2. Biosensors

Recently, plasmonic hot electrons were employed for biosensing.<sup>89–92</sup> One design is the utilization of plasmonic hot electron current as the sensing signal. Adsorption of biomolecules can modulate the sensing signal by turn on or off the electron-transfer channel in the circuit. For example, Qiao *et al.* reported selective detection of bisphenol A (BPA) in drinking water and liquid milk samples with a label-free photoelectrochemical aptasensor,<sup>89</sup> as illustrated in Fig. 8(a). Under light illumination, the Au/ZnO heterojunction exhibited a higher photocurrent than that of a pure ZnO nano-pencil, which was induced by plasmonic hot electrons from the excited Au nanoparticles. Selectivity was achieved by specific binding of BPA to its aptamer. When BPA was present in the assay, binding of aptamer to Au resulted in the blockage of photogenerated electron-transfer channels. Such a photoelectrochemical aptasensor showed a linear relationship with the BPA concentration in the range of 1–1000 nmol L<sup>-1</sup> at a limit of detection (LOD) of 0.5 nmol L<sup>-1</sup>. In addition, plasmonic hot carriers can be used for improving the sensitivity of electrochemical sensors. Plasmonic hot carriers can participate in the anodic oxidation or cathodic reduction, enhancing the electrochemical current. On the other hand, in the plasmonic metal/semiconductor composite structure, the plasmonic hot electron injected into the semiconductor from the metal can improve the charge carrier concentration, improving the responsive current of the sensor. For example, a plasmon-enhanced glucose electrochemical sensor was constructed based on the plasmon-accelerated electrochemical reaction (PAER) mechanism.<sup>91</sup> In this sensor [Fig. 8(b)], the energetic hot carriers were generated on the Au NP surface. At a suitable voltage, hot holes can be effectively depleted by oxidation of glucose due to their matched energy levels, which would effectively inhibit the electron–hole recombination. Thus, the generated hot electrons would be driven to the external circuit, producing an observable current. Because the PAER system is Schottky-junction-free, the hot carriers can be harnessed more efficiently, ensuring a higher efficiency toward glucose electro-oxidation. As a result, when LSPR was excited, the photocurrent increased due to glucose electro-oxidation

induced by LSPR [Fig. 8(c)]. As a result, this biosensor showed an improved sensitivity and LOD [Fig. 8(d)].

## B. Photodetection

Photodetectors are designed to transform the incident light (in a specific spectral range) into an electrical signal. The operating principle is based on the photovoltaic effect or photoconductivity modulation. In particular, the field-effect transistor (FET) was introduced for highly efficient photodetection. Because photodetectors are made of semiconductors such as Si, Ge, InGaAs, and PbS, the sensitive wavelength bandwidth is limited by the fixed bandgap of the specific semiconductors. To tune or extend the photodetection spectral range of detectors, hot electrons are utilized to enhance or generate the internal photoemission in photodetectors.<sup>93</sup> In addition, plasmonic hot electrons can be involved into photocurrent to enhance the photo-response intensity, leading to an improvement in sensitivity of detectors.

### 1. Internal photoemission

The Schottky diode and the Metal–Insulator–Metal (MIM) diode are two common structures used for internal photoemission. In the former structure,<sup>94</sup> a Schottky barrier ( $\Phi_B$ ) is formed at the metal/semiconductor interface. When incident photon's energy ( $E = h\nu$ ) is larger than the Schottky barrier height, plasmonic hot electrons can be injected into the semiconductor across the barrier [Fig. 9(a)], generating a photocurrent. The photodetection limit is determined not only by the bandgap of semiconductors but also by the height of the Schottky barrier. Generally, the Schottky barrier height is less than 1 eV, which is determined by the difference between the work function of the metal and the electron affinity of the semiconductor.<sup>95</sup> Thus, the plasmonic hot electron injection mechanism can be used to extend the detection bandwidth of the photodetector. In the MIM structure shown in Fig. 9(b),<sup>96,97</sup> the insulator interlayer is very thin, and hot electrons in the top metal can tunnel through into the bottom metal via the quantum tunneling effect and vice versa to produce a photocurrent. By creating asymmetric absorption or asymmetric barrier heights formed by using

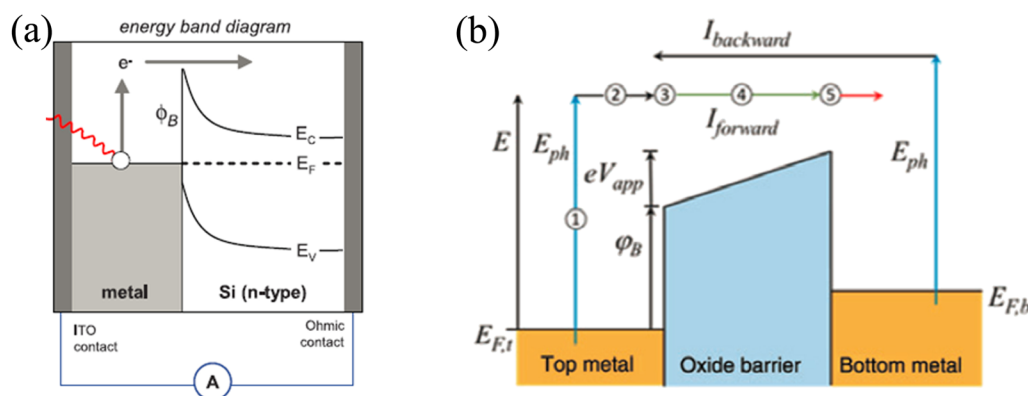


**FIG. 9.** Two types of photodetectors based on internal photoemission. (a) Schottky emission. Adapted with permission from Knight *et al.*, *Science* **332**, 702 (2011). Copyright 2011, American Association for the Advancement of Science. (b) Metal–insulator–metal emission. Adapted with permission from Chalabi *et al.*, *Nano Lett.* **14**, 1374 (2014). Copyright 2014, American Chemical Society.

different metals or applying a bias,<sup>98</sup> the tunneling current from one side to the other is thus dominant, leading to a measurable net current. In the MIM model, the insulator layer can be replaced with a semiconductor layer. In addition, one of the metal layers can be changed into a transparent conducting oxide layer with a similar physical working principle to the true MIM case.<sup>99–101</sup> However, the internal quantum efficiency in internal photoemission is very low, limiting their applications. The low efficiency is ascribed to the weak light absorption of the metal, which consequently induces a small quantity of low energy hot electrons, and huge energy losses for hot electrons during diffusion in the metal and across the interface.

The energy and momentum distribution of the plasmonic hot electrons can be tuned by the size, shape, and medium. In this way, the responsivity peak, bandwidth, and polarization dependence

of the device based on the plasmonic hot-electron internal photoemission can be tuned by controlling the SPR of the metal nanostructures.<sup>102</sup> By taking advantage of great tunability of plasmon, various photodetectors have been developed based on different plasmonic modes such as LSPR,<sup>103–105</sup> SPP excitations,<sup>106</sup> grating-coupling,<sup>102,107,108</sup> waveguides,<sup>109–113</sup> and plasmonic MIM structure.<sup>97,99,114,115</sup>

## 2. LSPR-based Schottky diode photodetector

Plasmonic nanoparticles can serve as light antennas by utilizing LSPR, generating a large number of energetic hot electrons to enable sub-bandgap photodetection.<sup>103,116–118</sup> For example, Knight *et al.* demonstrated a photodetector based on an Au nanorod array as a plasmonic nano-antenna on a silicon substrate with the ability to detect near-infrared light ( $1.2\ \mu\text{m}$ – $2.5\ \mu\text{m}$ ) [Fig. 10(a)].<sup>103</sup> By

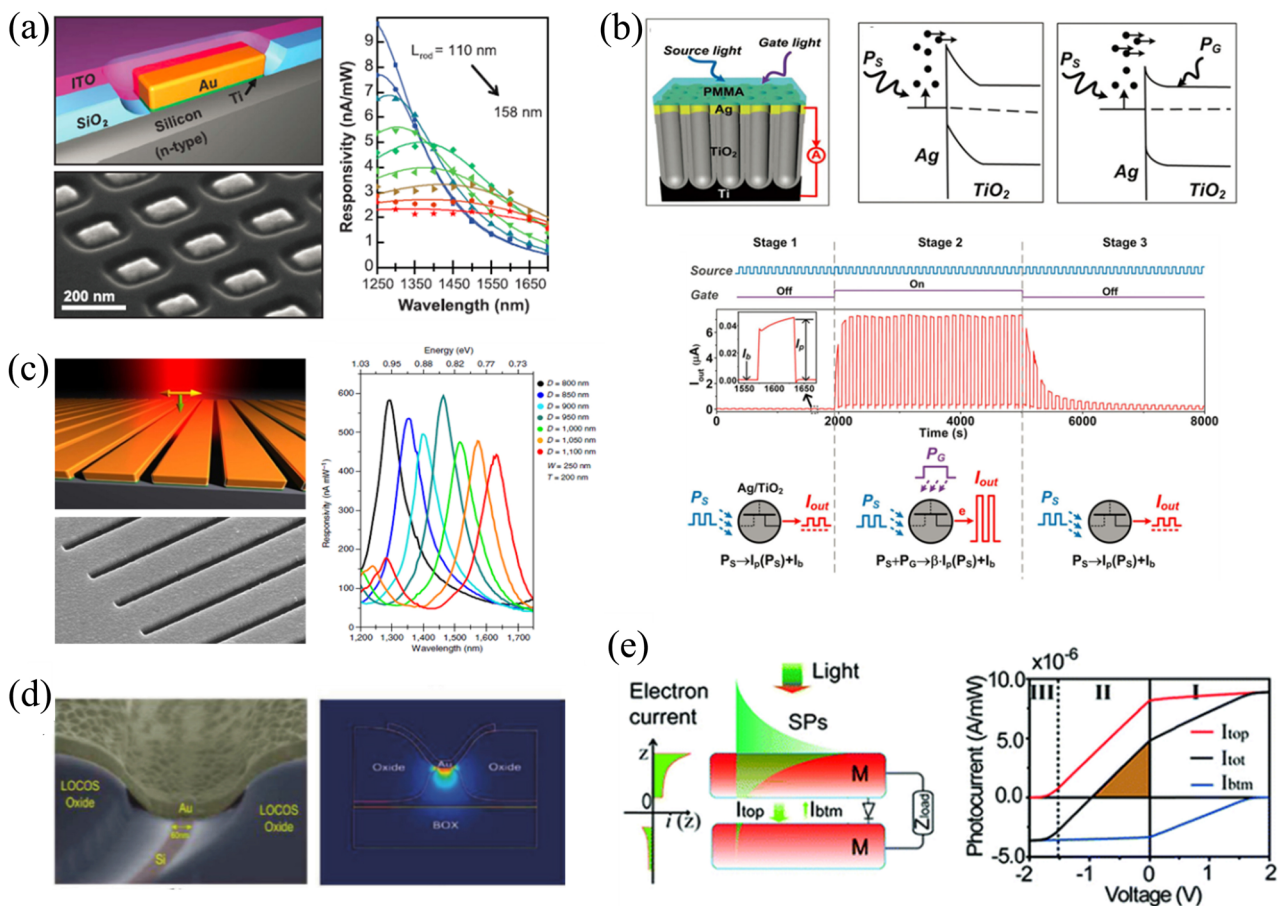


**FIG. 10.** Internal photoemission photodetector based on plasmonic hot electron transfer. (a) Schematic and SEM of the Au nanorods as the plasmonic nano-antennas on the silicon substrate. The photocurrent can be modulated by the antenna length. Adapted with permission from Knight *et al.*, *Science* **332**, 702 (2011). Copyright 2011, American Association for the Advancement of Science. (b) Photocurrent modulated by the height of the Schottky barrier in a porous Ag/TiO<sub>2</sub> array detector. Adapted with permission from Gao *et al.*, *Adv. Funct. Mater.* **28**, 1802288 (2018). Copyright 2018, WILEY-VCH Verlag GmbH & Co. (c) A gold grating on an *n*-type silicon substrate, achieving linear modulation of the response peak in a broad wavelength region by tuning the grating parameter. Adapted with permission from Sobhani *et al.*, *Nat. Commun.* **4**, 1643 (2013). Copyright 2013, Macmillan Publishers Limited. (d) A silicon waveguide-based SPP Schottky photodetector. Adapted with permission from Goykhman *et al.*, *Nano Lett.* **11**, 2219 (2011). Copyright 2011, American Chemical Society. (e) Schematic design of the MIM device. A net photocurrent ( $I_{\text{top}} - I_{\text{bot}}$ ) can be achieved due to the plasmonic hot-electron density difference in the two electrodes. Adapted with permission from F. Wang and N. A. Melosh, *Nano Lett.* **11**, 5426 (2011). Copyright 2011, American Chemical Society.

tuning the geometry of the Au nanorods (aspect ratio), the SPR absorption spectrum and the photoresponsivity can be modulated. Gao *et al.* also directly showed that changing the barrier height could modulate the photocurrent in a porous Ag/TiO<sub>2</sub> array-based near-infrared photodetector [Fig. 10(b)].<sup>117</sup> They found that a Schottky barrier was formed by chemisorbed oxygen and could be reduced by reducing the amount of chemisorbed oxygen using ultraviolet (UV) light as the gate input. In this way, the height of the Schottky barrier could be modulated by the extra gate light illumination, resulting in several to one hundred times enhancement of plasmon-induced photocurrent. Pescaglini *et al.* reported an Au nanorod–ZnO nanowire hybrid system, showing a large photoresponse under light irradiation in the spectral range of 650–850 nm, accompanied by an “ultrafast” transient photoresponse at a timescale of 250 ms.<sup>118</sup>

### 3. Plasmonic waveguide-based photodetector

In gratings with periodically spaced slits or a nanohole array, the incident light can be coupled strongly to SPP, leading to strong and resonant absorption. The absorption frequency can be modulated by the nanostructure parameters such as the periodicity and slit dimension. When a grating array is combined with the semiconductor substrate, photocurrent will be generated due to the SPP-induced hot electron ejection from the metal to semiconductor.<sup>102,107,108</sup> For example, Sobhani *et al.* reported a grating-based photodetector device,<sup>102</sup> consisting of Au gratings on an *n*-type silicon substrate [Fig. 10(c)]. It showed 0.6 mA W<sup>-1</sup> without an external bias at an internal quantum efficiency of ~0.2%, which was 20 times larger than that of the nano-antenna-based device. Additionally, the wavelength-dependent spectrum was three times narrower than the nano-antenna-based device. By tuning the grating parameter, it was easy to linearly tune the responsivity peak between 1295 nm and 1635 nm. This tunability opens up the possibility for the design and fabrication of the plasmonic detector driven in a narrow bandwidth of infrared light.

A waveguide-based photodetector design can produce higher internal quantum efficiency than antenna-based designs.<sup>95,109–113</sup> Because SPPs propagate and excite hot electrons along with the metal/dielectric interface, a shorter diffusion pathway is expected for hot electron injection into the semiconductor. Moreover, the electric field component of SPPs can be perpendicular to the Schottky interface. Consequently, the generated hot electrons preferentially have a momentum component perpendicular to the metal/dielectric interface, which improves the hot electron transfer probability. For example, Goykhman *et al.* reported a silicon waveguide-based SPP Schottky photodetector [Fig. 10(d)].<sup>109</sup> The photodetector was fabricated on an insulator substrate using a self-aligned approach of local oxidation of silicon. It showed an internal responsivity of 0.25 mA/W and 13.3 mA/W under irradiation at wavelengths of 1.55 μm and 1.31 μm, respectively.

### 4. Plasmonic MIM photodetector

In MIM photodetectors, one of the metal layers can be replaced with a plasmonic metal nanostructure. Plasmonic hot electrons will be generated and subsequently tunnel across the thin oxide insulator layer to the other metal film to produce a photocurrent. These detectors can operate without an external bias at room temperature. For example, Melosh *et al.* presented a simple plasmonic MIM

device [Figs. 10(e)],<sup>97</sup> consisting of three films of Au (35 nm)–Al<sub>2</sub>O<sub>3</sub> (4 nm)–Au (30 nm). A Kretschmann prism configuration was applied to couple the incident light to the top electrode, resulting in asymmetric absorption and abundant hot electrons. These hot electrons tunneled from the top electrode to the bottom. Later, Chalabi *et al.* re-shaped the top Au film into a striped antenna to create a stronger LSPR,<sup>114</sup> thus most of the incident light absorbed in the top electrode. A photocurrent could be measured even without an external bias.

### 5. Plasmonic FET photodetector

Recently Kojori *et al.* reported a plasmon-modulated field-effect transistor (FET) photodetector based on a back-gated thin film transistor with a plasmonic metal nanostructure (Fig. 11).<sup>119,120</sup> Plasmonic Au nanoparticles were incorporated into the active channel of the transistor, consisting of a source, drain, and gate, as shown in Fig. 11(a). The plasmon-induced hot electrons were injected into the ZnO film channel, consequently increasing the channel conductivity and drain current. As a result, the drain current can be modulated by applying an external electric field and varying the gate voltage [Fig. 11(b)]. Without a gate voltage bias, only the plasmon-induced hot electrons, which possess sufficient energy for overcoming the interfacial Schottky barrier, can be injected into the semiconductor and collected as the drift current. With a gate voltage bias, an electron accumulation layer (*n*-channel) was formed inside the semiconductor layer close to the mediator layer. The spatial variation in electron density generated a large potential gradient from the floating ground (metal nanostructure) to the electron accumulation region. The internal electric field created by the gate bias facilitated the electrons to move to the other boundary where the FET channel was located. The migrating hot electrons were driven by the gate voltage, contributing to the channel enhancement and allowing more drain current to flow.

### C. Solar energy conversion

To address the grand challenges in energy and ecology sustainability,<sup>121</sup> increasing efforts are being made to develop photovoltaic devices, photocatalysts, and photoelectrochemical cells (PECs).<sup>122</sup> Although organic perovskites and tandem-structured inorganic III–V compounds have achieved a high solar conversion efficiency, they are expensive or/and unstable in operation. Hence, alternative materials such as silicon and metal oxides are still under development for solar energy devices. These materials cannot meet all the requirements for practical applications due to one or more shortcomings among large bandgap, low charge mobility, high-density surface trap states, and indirect bandgap feature. For example, wide bandgap semiconductors such as TiO<sub>2</sub> are stable and inexpensive, but they can only absorb UV light, which accounts for only ~5% of solar radiation.

To extend the light absorption spectral range and to improve the energy conversion efficiency of semiconductors, plasmonic metal nanostructures are incorporated with semiconductors to form heterojunctions. Plasmonic metal nanostructures can adsorb visible-light or infrared light and transfer plasmonic energy to the semiconductors, enhancing the charge separation and migration in the semiconductor. As summarized in Ref. 11, the plasmon enhances photoconversion in a metal–semiconductor heterojunction via three

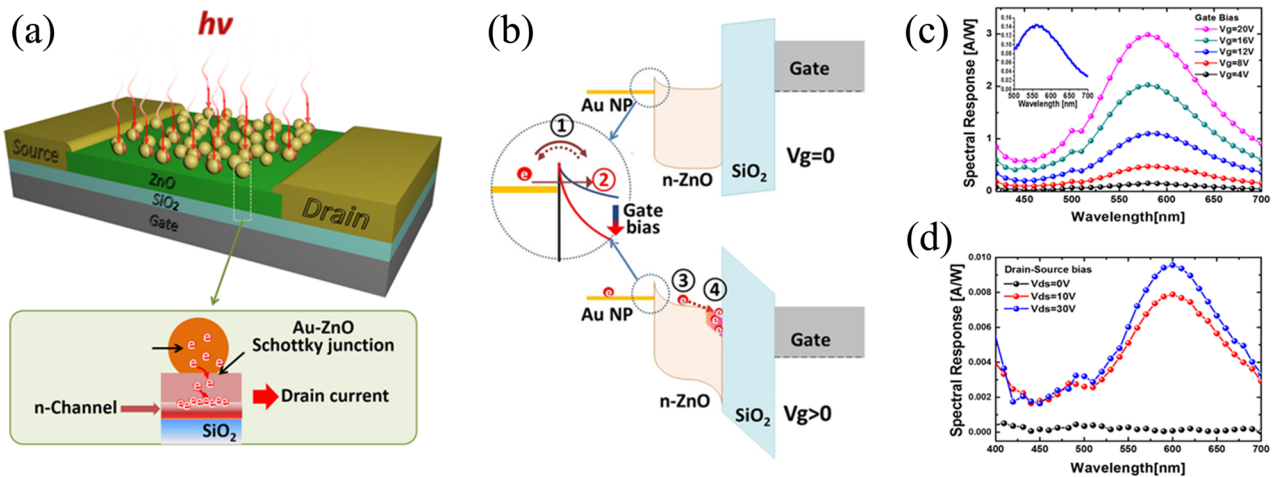


**FIG. 11.** Photodetectors based on the plasmonic FET. (a) Typical structure and operating principle. (b) Thermionic diffusion without a gate bias, while the internal field-assisted hot electron migration and quantum tunneling at the Schottky junction with a gate voltage bias. (c) Spectral response under different gate voltage biases. The inset shows the absorption spectrum of Au nanoparticles on a ZnO film/glass substrate with a drain–source bias voltage of 20 V. (d) Spectral response with different drain–source voltages without a gate voltage bias. Adapted with permission from Kojori *et al.*, *Nano Lett.* **16**, 250 (2016). Copyright 2015, American Chemical Society.

plasmonic energy transfer mechanisms, light scattering/trapping, plasmon-induced resonance energy transfer (PIRET), and hot electron injection. Wu *et al.* revealed that the balance between three mechanisms depends on the plasmon dephase and predicted the theoretical maximum efficiency of solar energy conversion in plasmonic metal–semiconductor heterojunctions.<sup>14,15</sup>

If a plasmonic metal nanostructure is utilized to absorb incident light in an extended spectral range and to transfer the absorbed light energy to adjacent molecules or semiconductors, this nanostructure is called “plasmonic photosensitizer.”<sup>11,30</sup> This section is focused on the hot electron injection mechanism and shows how to enhance photovoltaic and photocatalytic performance with plasmonic photosensitizers.

### 1. Photovoltaic devices utilizing plasmonic hot carriers

In nature, both photovoltaic devices and photocatalysis require two common steps: light harvesting and charge separation. In most cases of plasmonic solar cells, plasmonic metals are used as light antennas for light scattering/trapping to improve photovoltaic performance by enhancing light harvest, whereas application of the plasmonic hot carrier transfer mechanism is limited for the low transfer efficiency.<sup>123,124</sup> To utilize hot carriers effectively, at least three factors need to be considered: (i) incident light can efficiently excite hot carriers in the plasmonic metal nanostructure, (ii) plasmonic hot carriers are efficiently separated and extracted before they are cooled to the equilibrium state, and (iii) recombination including thermal relaxation and charge back transfer is suppressed as far as possible. Meeting the three conditions cannot guarantee a high energy transfer efficiency. The excited hot electrons suffer fast relaxation at the timescale of hundreds of femtoseconds and the interface barrier of the metal/semiconductor, resulting in only a small percentage of hot electrons that can be effectively extracted to the semiconductor.<sup>21,63,125</sup> Therefore, it is essential to construct an

appropriate interface to enable rapid charge separation and transfer. A sandwich structure, electron transport material/plasmonic metal/hole transport material, is a typical design for a plasmonic photovoltaic device. Generally, *n*-type semiconductors (e.g., TiO<sub>2</sub>) are used for hot electron collection and transport, while *p*-type semiconductor or other hole transport materials such as poly(*N*-vinylcarbazole) (PVK) are used for hot hole collection and transport.

A Schottky junction consisting of the semiconductor and plasmonic metal nanostructure is the start point for harvesting hot electrons. For example, Konstantatos *et al.* designed a metal/insulator/semiconductor heterostructure [Fig. 12(a)]<sup>126</sup> in which the Ag nanostructure electrode can generate LSPR and the 1 nm thick Al<sub>2</sub>O<sub>3</sub> space layer can passivate the interface states. In this photo-diode device, plasmonic hot electrons can enter TiO<sub>2</sub> across the Au/Al<sub>2</sub>O<sub>3</sub>/TiO<sub>2</sub> Schottky junction or through the Schottky emission, forming photocurrent [Fig. 12(b)]. This plasmonic device has achieved an open-circuit voltage of 0.5 V, a fill-factor of 0.5, and a power conversion efficiency of 0.03% when using the nano-patterned Ag electrode. In addition, Mubeen *et al.* demonstrated a plasmonic photovoltaic device using the Au nanorod array/TiO<sub>2</sub>/Ti sandwich structure.<sup>127</sup> An open-circuit voltage of 210 mV was achieved with this plasmonic photo-diode device at a 50 nm thick TiO<sub>2</sub> layer.

However, if only the Schottky junctions are utilized for separating charges that come from the plasmonic metal, the overall solar energy conversion efficiency of photovoltaic devices is too low. Therefore, the plasmonic hot electron injection process is used to enhance the performance of conventional photovoltaic devices, such as organic photovoltaics, Si solar cells, and dye-sensitized solar cells (DSSCs). For example, Au nanoparticles were embedded at the hole-conductor/semiconductor (spiro-OMeTAD/TiO<sub>2</sub>) interface in a solar cell [Fig. 12(c)].<sup>128,129</sup> The Au nanoparticle played multiple roles. One of the roles was that the Au nanoparticles served



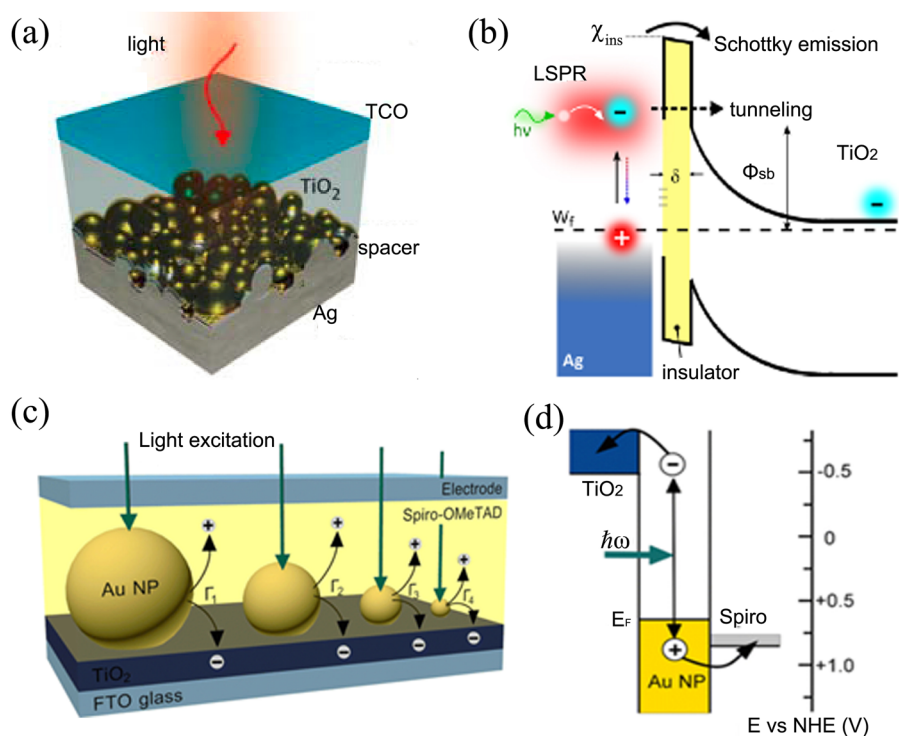


**FIG. 12.** Photovoltaic device utilizing plasmonic hot electron injection. (a) Schematic illustration of a metal/insulator/semiconductor heterostructures. (b) The operating principle of the heterostructure in (a). Adapted with permission from de Arquer *et al.*, ACS Nano 7, 3581 (2013). Copyright 2013, American Chemical Society. (c) Solar cell with Au nanoparticles at the TiO<sub>2</sub>/spiro-OMeTAD interface. (d) Role of Au nanoparticles in the device in (c). Adapted with permission from Reineck *et al.*, J. Phys. Chem. Lett. 7, 4137 (2016). Copyright 2016, American Chemical Society.

as photosensitizers [Fig. 12(d)] in which the plasmonic hot electrons were injected to TiO<sub>2</sub> and hot holes were transferred to spiro-OMeTAD (hole-conductor). The overall performance of the device was improved when the Au particle size was reduced from 40 nm to 5 nm, achieving a maximum absorbed photon-to-electron conversion efficiency (APCE) or an internal quantum efficiency (IQE) of 13.3%. Recently, the plasmonic Ag@TiO<sub>2</sub>@Pa (benzoic-acid-fullerene bishell) sandwich nanoparticles were embedded in the active layer in a solar cell in which plasmonic hot electrons were extracted to the fullerene in the Pa, contributing to the photocurrent.<sup>130</sup> The Pa outer-shell was important to extract the charge; otherwise, the charge carriers would be trapped inside the nanoparticles without it. As a result, addition of plasmonic sandwich nanoparticles into the organic solar cell achieved a maximum power conversion efficiency of 13.0%, which enhanced the performance by 12.3%. Moreover, Zhang *et al.* introduced the Au-TiO<sub>2</sub> composite into an organic photovoltaic device,<sup>131</sup> which exhibited a notably enhanced transient photogenerated voltage peak of 0.56 V under light irradiation at 600 nm because of the plasmonic hot electron injection into TiO<sub>2</sub>. The group of Xiong also integrated the Ag nanoplates into a Si-based solar cell, Si-poly(3,4-ethylene dioxythiophene)/poly(styrene sulfonate) (PEDOT:PSS).<sup>132</sup> Hot electrons were generated in the Ag nanoplates at wavelengths of 550–1100 nm and transferred to the CB of Si. As compared with pristine photovoltaic cells, the current density and power conversion efficiency were improved by 28% and 40%, respectively, after addition of the Ag nanoplates. Plasmonic Au-TiO<sub>2</sub> core-shell structured photoanodes (Au@TiO<sub>2</sub>, SiO<sub>2</sub>@TiO<sub>2</sub>@Au, and SiO<sub>2</sub>@Au@TiO<sub>2</sub>) have also been developed to improve DSSCs performance.<sup>133,134</sup>

## 2. Photocatalysts utilizing plasmonic hot carriers

With the excited hot carriers, a plasmonic metal can directly photocatalyze a chemical reaction on the surface or serves as a photosensitizer with the semiconductor to improve the photocatalysis performance. Typically, in the direct photocatalysis by a plasmonic metal nanostructure (metal-adsorbate complexes), the direct transfer pathway of hot carriers such as CID could be predominant [Figs. 2(b) and 3].<sup>11,34</sup> In metal-adsorbate complexes, SPR-mediated hot electrons can be injected into specific electronic states of molecules adsorbed on the surface of plasmonic metals. Alternatively, the occupied electrons in the adsorbate could be injected into the metal and recombine with the hot holes, i.e., the plasmonic hot holes may oxidize the adsorbate.<sup>91,135–138</sup> The hot carrier injection induces various physicochemical processes such as molecular dissociation, desorption, or chemical reactions.<sup>85,139</sup> For example, hot electrons can be injected from the Au nanoparticles into the antibonding orbital ( $1\sigma_u^*$ ) of the adsorbed H<sub>2</sub> molecule, leading to H<sub>2</sub> dissociation [Fig. 13(a)].<sup>85</sup> Indeed, dissociation of H<sub>2</sub> molecules was observed by exposing the Au nanoparticles to a mixture of H<sub>2</sub> and D<sub>2</sub>. The HD formation efficiency showed an instantaneous sixfold improvement under the laser excitation of the plasmon. The time-domain time-dependent density functional theory (TDDFT) and Ehrenfest dynamics simulations have also confirmed this process.<sup>140</sup> However, this process was suppressed due to sequential charge transfer when the H<sub>2</sub> molecule was located in the center of gap between the plasmonic metal dimer. Mukherjee,<sup>141</sup> Landry<sup>142</sup> and their co-workers prepared the Au nanoparticles and the Ag nanocubes for plasmonic activation of H<sub>2</sub> splitting,

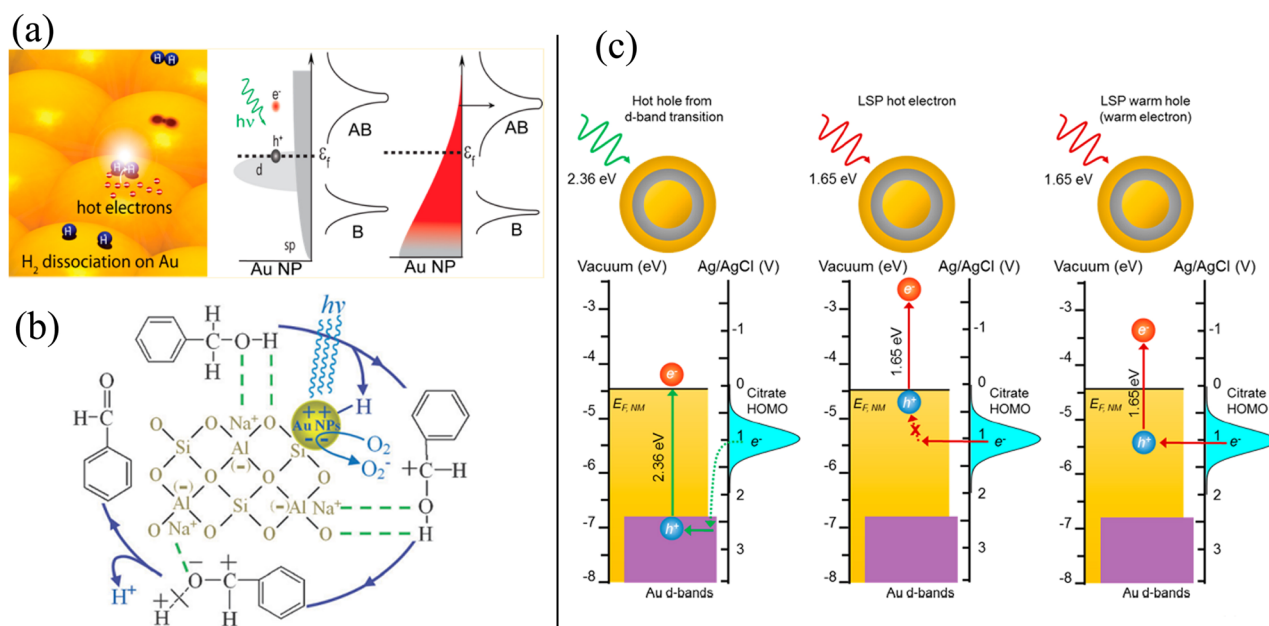


**FIG. 13.** Proposed mechanisms for plasmon-modulated photochemical reactions. (a) Dissociation of H<sub>2</sub> molecules on plasmonic Au nanoparticles. Adapted with permission from Mukherjee *et al.*, *Nano Lett.* **13**, 240 (2013). Copyright 2012, American Chemical Society. (b) Photo-oxidation of benzyl alcohol molecules through hot carrier transfer. Adapted with permission from Zhang *et al.*, *Chem. - Eur. J.* **18**, 8048 (2012). Copyright 2012, Wiley-VCH Verlag GmbH & Co. (c) Energy diagrams depicting hot hole-mediated citrate oxidation. A 2.36 eV excitation resulted in the formation of hot holes in the Au d-bands, which allowed electron transfer from the citrate ion HOMO exergonically. However, hot holes were generated via plasmon decay from a 1.65 eV excitation and efficiently transferred if their energetic level was overlapped with the citrate HOMO level, leading to oxidation of the citrate ions. Adapted with permission from Schather *et al.*, *J. Phys. Chem. Lett.* **8**, 2060 (2017). Copyright 2017, American Chemical Society.

respectively. When the plasmonic materials were excited by light, transient charge carriers were generated at the surface. The resulting hot electrons were transferred to the adsorbed H<sub>2</sub> molecules to drive the dissociation of molecules.

It is interesting that plasmonic nanoparticles can catalyze polymerization.<sup>143,144</sup> In this process, plasmonic hot electrons induced the binding of an olefin monomer onto the Au nanoparticle surface and generated the radicals. The radical modulated the polymerization, leading to a polymer coating on the metal nanoparticle. *In situ* polymerization on plasmonic nanostructures could open a new avenue for patterning polymers on the nanoscale. Moreover, environmental organic contaminants can be decomposed on plasmonic metal nanoparticles via hot carrier injection to organic compounds.<sup>11</sup> Zhang *et al.*<sup>145</sup> prepared Au nanoparticles on the zeolite support for selective photo-oxidation of benzyl alcohol to aldehydes, as shown in Fig. 13(b). The electronic polarization of the plasmon-excited Au nanoparticles was proposed to induce a high electronegativity for abstracting protons from the cleavage of C–H bonds in benzyl alcohol molecules. In addition, plasmonic hot electrons on Au nanoparticles were transferred to molecular oxygen to produce activated superoxide radicals (O<sub>2</sub><sup>•-</sup>), leading to decomposition of benzyl alcohol molecules. In addition, plasmonic Au nanoparticles showed photocatalytic activity toward the multi-electron and multi-proton reduction of CO<sub>2</sub>.<sup>146</sup> The results show that plasmonic hot electrons drove the formation of the C1 and C2 hydrocarbons on the Au nanoparticle surface. Moreover, ionic liquids can stabilize

the high-energy CO<sub>2</sub><sup>•-</sup> radical intermediates formed at the nanoparticle/solution interface and facilitate the hot electron transfer from the Au nanoparticle to the adsorbed CO<sub>2</sub> molecules.<sup>147</sup> Recently, increasing attention was paid to the photocatalytic oxidation of plasmonic hot holes.<sup>135–138</sup> For example, Schlather *et al.* investigated the hot hole-induced oxidation of citrate ions on the Au@SiO<sub>2</sub>@Au core-shell nanoparticle electrode [Fig. 13(c)].<sup>135</sup> They found that charge transfer to the adsorbed citrate was most efficient at high photon energies. However, hot holes generated via plasmon decay can also oxidize the citrate if their energetic level is overlapped with the citrate HOMO level.

In the above-mentioned plasmonic metal/adsorbate systems, plasmonic hot electrons are injected into the reactants and get involved in a chemical reaction, where the plasmonic metals serve as the active reaction sites. To extend the photocatalysis application of plasmonic metals, metal/metal heterostructures have been designed toward the selective catalysis of specific reactions. For example, Zheng *et al.* designed a plasmonic Au/Pt heterojunction photocatalyst<sup>138</sup> in which Pt nanoparticles were decorated on the two ends of individual Au nanorods. Plasmonic hot electrons, which were excited in the Au nanorods, were transferred to the Pt nanoparticles, driving water reduction to hydrogen. Meanwhile, hot holes were extracted out of the Au nanorods to drive methanol oxidation. The heterostructure facilitated the separation of electrons from holes and improved surface catalysis for hydrogen evolution. In addition, Aslam *et al.* prepared the Ag@Pt core@shell (75 nm@1 nm)

nanocube photocatalyst toward CO oxidation in the presence of excessive  $H_2$ .<sup>149</sup> The ultrathin Pt outer-shell reduced the light scattering and increased the light absorption in the Ag core, which resulted in excitation of more hot electrons. Hot electrons were transferred to the Pt where the active reaction sites were present. Moreover, Halas *et al.* prepared the heterometallic antenna-reactor complexes (Al nanocrystals decorated with multiple smaller Pd or Ir islands, Cu–Ru surface alloy).<sup>150–152</sup> In the Au–Pd complex, the supralinear power dependence suggested that the hot carriers induced  $H_2$  desorption at the Pd island surface under light illumination. When acetylene was present along with  $H_2$ , the production selectivity for ethylene relative to ethane was strongly enhanced, approaching 40:1.

In plasmonic metal–semiconductor heterostructures, plasmonic hot carriers transfer into the semiconductor through either a direct or an indirect transfer pathway,<sup>11</sup> where the semiconductor serves as the active reaction site. A suitable band alignment between the metal and the semiconductor can facilitate the extraction of plasmonic hot carriers and participation in the catalytic reaction on the semiconductor surface. Nishijima *et al.* deposited a gold nanorod pattern on the  $TiO_2$  film as the photoanode in a PEC<sup>56</sup> in which hot electrons were injected into  $TiO_2$  and hot holes were extracted

to oxidize water molecules. The presence of an Au nanorod array on  $TiO_2$  extended the light absorption range from the UV light to the near-infrared light region, and the photocurrent was generated in the spectral range up to 1200 nm. Primo *et al.*<sup>153</sup> demonstrated the enhanced photocatalytic oxygen generation by depositing Au nanoparticles on ceria ( $CeO_2$ ).  $CeO_2$  is a wide bandgap semiconductor that cannot be excited by visible-light irradiation. However, the oxygen evolution rate reached  $10.5 \text{ mmol h}^{-1}$  for the gold-supported  $CeO_2$  particles under visible-light illumination. The visible-light photocatalytic activity was attributed to the injection of hot electrons from the Au photosensitizer into the CB of  $CeO_2$ . The holes from the Au nanoparticles drove the water oxidation reaction to produce oxygen gas. In addition, Chen and co-workers<sup>73</sup> synthesized the gold nanospheres on a ZnO nanorod array, which served as a photoanode in a PEC. The photocurrent under visible-light illumination was ascribed to hot electron injection to ZnO from the gold nanospheres [Fig. 14(a)]. The Fowler theory was utilized to evaluate the number of photoelectrons with enough energy to overcome the Schottky barrier at the Au/ZnO interface. Figure 14(b) shows the photocurrent as a function of the wavelength of incident light, which partially matched Fowler's law. Nevertheless, the photocurrent diverged from Fowler theory with the deviation, which was associated with LSPR.

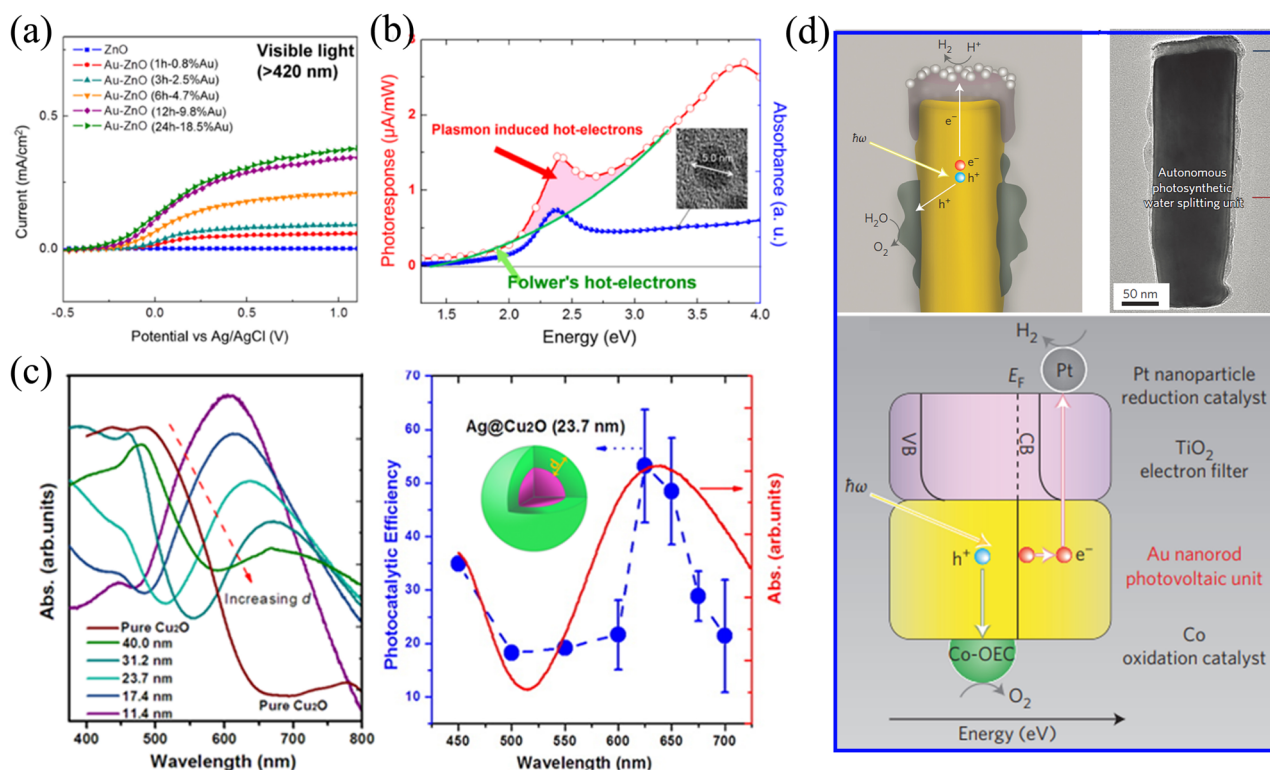


**FIG. 14.** (a) Linear-sweep voltammogram of Au–ZnO nanorod array photoelectrodes in a 0.5M  $Na_2SO_4$  electrolyte. (b) The absorption spectrum and photocurrent action spectrum of Au–ZnO nanorod array photoelectrodes, fitted to Fowler's law. Adapted with permission from Chen *et al.*, ACS Nano 6, 7362 (2012). Copyright 2012, American Chemical Society. (c) The light absorption spectra and the photocatalysis action spectrum of Ag@Cu<sub>2</sub>O core-shell nanoparticles. Adapted with permission from Wu *et al.*, ACS Catal. 3, 47 (2013). Copyright 2014, American Chemical Society. (d) Structure and energy level diagram of the autonomous photosynthetic device. Adapted with permission from Mubeen *et al.*, Nat. Nanotechnol. 8, 247 (2013). Copyright 2013, Macmillan Publishers Limited.

The results indicated that photocurrent was dominantly composed of hot electron flow and enhanced by LSPR.

The mean-free path of hot electrons in a metal is approximately 20–30 nm.<sup>70</sup> The previous studies also showed that rapid charge recombination ( $<1$  ns) occurred between the injected hot electrons in the semiconductor and the holes in the plasmonic metal in Au/TiO<sub>2</sub>.<sup>50,52</sup> Hence, it is important to mitigate trapping and recombination of hot carriers in photocatalysts. In many cases, plasmonic metals were synthesized with capping ligands, which act as the electrical resistors for charge transfer. Recently, the ligand-free Au nanoparticles were coupled to TiO<sub>2</sub> for photocatalytic dye degradation and hydrogen evolution.<sup>154,155</sup> Besides the plasmonic metal surface, the distribution and architecture of plasmonic metal nanoparticles and semiconductors in heterojunctions also need to be considered in design. In a conventional heterojunction structure, metal nanoparticles are randomly distributed in the crystal domains of the semiconductor. The disordered crystal domains cause additional energy loss during the hot-electron transfer process. In contrast, Bian *et al.* synthesized a TiO<sub>2</sub> superstructure with an ordered configuration,<sup>61</sup> which provided an efficient charge migration pathway, suppressing the charge recombination. Time-resolved diffuse reflectance spectroscopy revealed that the time constant for electron accumulation in the Au/meso-TiO<sub>2</sub> system was 5.6 min, which was much longer than the conventional counterparts. This was responsible for an improved photocatalytic activity toward organics degradation and hydrogen generation. In addition, Li *et al.* revealed that a core@shell structure of plasmonic metal@semiconductor nanoparticles allowed for strong coupling between the plasmonic metal core and the semiconductor shell.<sup>156</sup> As compared to the Ag core alone, the Ag@Cu<sub>2</sub>O nanoparticles exhibited an extraordinarily large red-shift in the LSPR band due to the high refractive index of Cu<sub>2</sub>O, and the LSPR band can be tuned sensitively by tailoring the Cu<sub>2</sub>O shell thickness [Fig. 14(c)]. As a result, the optimized Ag@Cu<sub>2</sub>O composite nanoparticles showed a largely extended light absorption spectral range as compared to Cu<sub>2</sub>O alone. Indeed, the light absorption spectral range of the Ag@Cu<sub>2</sub>O core-shell

nanoparticles covered the entire visible-light region. Owing to the large intimate metal/semiconductor interfacial area, the Cu<sub>2</sub>O shell can effectively harness the plasmonic hot electrons from the Ag core and strongly interact with Ag through near-field coupling.<sup>156</sup> Therefore, the Ag@Cu<sub>2</sub>O core-shell nanoparticles exhibited extraordinary photocatalytic activity toward methyl orange decomposition under visible-light radiation [Fig. 14(c)], which was comparable to that under the UV-light illumination. It is worth noting that the plasmonic hot electron injection process does not occur alone in many cases. It may function along with other plasmonic energy transfer mechanisms such as PIRET to enhance the performance of materials and devices.<sup>156</sup>

Use of co-catalysts is an additional route to help the hot carrier extraction and to suppress the charge recombination. Mubeen *et al.*<sup>57</sup> prepared an autonomous photocatalytic water splitting device using the aligned gold nanorods as light antennas, capped with a TiO<sub>2</sub> layer to form a metal–semiconductor Schottky junction [Fig. 14(d)]. The TiO<sub>2</sub> cap was modified with platinum nanoparticles, which serves as the hydrogen evolution co-catalyst. The Au nanorod surface was decorated with a cobalt-based oxygen evolution catalyst (Co-OEC). Under visible-light irradiation, plasmonic hot electrons were injected from the Au nanorods to the TiO<sub>2</sub> layer and migrated to the Pt nanoparticles, driving the hydrogen evolution reaction. The hot holes in the Au nanorods were extracted to the Co-OEC catalyst, oxidizing water to oxygen gas. To suppress hot carrier recombination, another strategy has been developed to tailor the surface properties of a photocatalyst by controlling the selective exposure of different crystal facets.<sup>157,158</sup> The different facets of the photocatalyst showed varying catalytic performance due to the differences in the specific energy level of the facets. Accordingly, the oxidation and reduction co-catalysts were decorated on the different specific facets of the semiconductor, respectively. For example, Bai *et al.* specifically deposited the Ag and Pd nanoparticles on the (001) and (110) facets of the BiOCl photocatalyst, respectively.<sup>158</sup> In this design, the Ag nanoparticles served as the plasmonic light antennas, while the Pd nanoparticles acted as the co-catalyst. The spatial

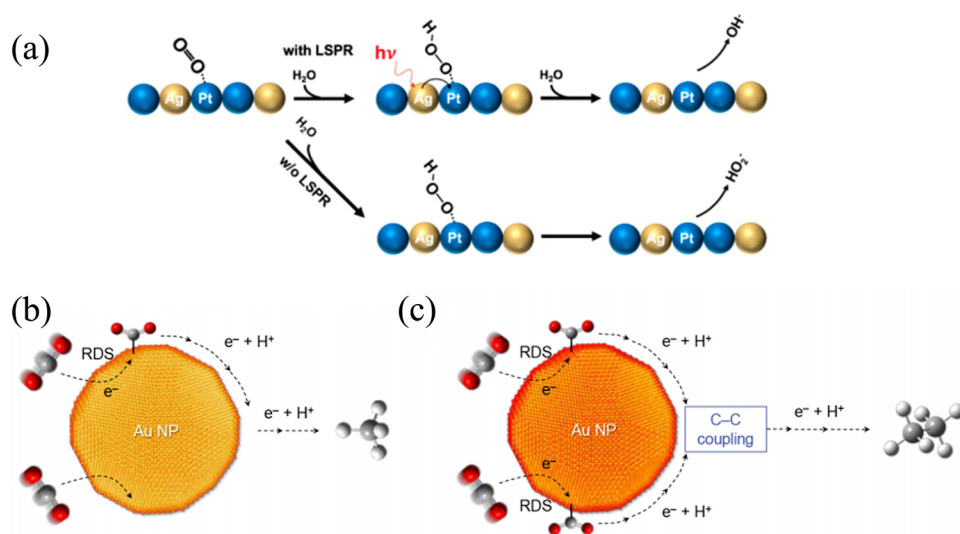


**FIG. 15.** (a) The suppression of peroxide yield in the oxygen reduction reaction via hot electron injection. Adapted with permission from Lin *et al.*, *J. Am. Chem. Soc.* **139**, 2224 (2017). Copyright 2017, American Chemical Society. [(b) and (c)] Light excitation influences hydrocarbon product selectivity. Adapted with permission from Yu *et al.*, *Nano Lett.* **18**, 2189 (2018). Copyright 2018, American Chemical Society.



distribution of metal nanoparticles on different facets improved the charge separation.

Selectivity is an important issue in heterogeneous catalysis. It is essential to fully control the reaction pathway, the product composition, and the chemical transformation yield. Hot carriers can be utilized to improve the selectivity of chemical reactions. The energy distribution of hot carriers can be tuned by the material, size, and shape of plasmonic nanostructures.<sup>34–36,159,160</sup> The tuned hot carriers can be injected into the specific energetic level of the reactants, achieving reaction selectivity. Boerigter *et al.* reported that the direct hot electron transfer process enabled selective chemical reactions through tuning the energetic level of hot electrons.<sup>34,36</sup> The oxygen reduction reaction (ORR) generally involves a four-electron transfer process to generate water. However, undesired by-products such as hydrogen peroxide ( $\text{H}_2\text{O}_2$ ) could be produced via a two-electron transfer pathway. To suppress the side reaction, the Ag–Pt bimetallic nanocages were prepared as the ORR catalysts [Fig. 15(a)].<sup>160</sup> The hot electrons transferred from Ag to Pt, which induced a higher electron population in the antibonding states of  $\text{O}_2$  adsorbates. The antibonding electron population facilitated the breaking of the O–O bonds in the  $\text{O}_2$  molecules and the production of desirable  $\text{H}_2\text{O}$ . Light intensity can also tune the product selectivity.<sup>146</sup> As shown in Fig. 15(b), hot electrons were transferred from the Au nanoparticle to the adsorbed  $\text{CO}_2$ , forming a radical ion intermediate,  $\text{CO}_2^{\bullet-}$  (or its hydrogenated form), which was the rate-determining step (RDS) for C1 generation. After a cascade of hot electron- and proton-transfer steps,  $\text{CH}_4$  was achieved. However, under high-intensity of light illumination, the hot electron transfer rate became large, and a multiple-electron transfer process took place within the surface-adsorbed  $\text{CO}_2$ , which activated two  $\text{CO}_2$  adsorbates simultaneously. The formed  $\text{CO}_2^{\bullet-}$  intermediate pair can undergo C–C coupling. As a result,  $\text{C}_2\text{H}_6$  was formed after a series of hot electron and proton transfer processes [Fig. 15(c)].

#### IV. REMARKS AND OUTLOOK

Research on plasmonics has made great progress in the past two decades. Discovery of new theories has advanced the fundamental understanding of plasmon and hot carriers (Fig. 16). In particular, TAS and XANES have made new discoveries or confirmed the theoretical predictions. Rapid development in synthesis and fabrication techniques has resulted in the availability of systematically designed plasmonic materials and devices, which has not only widened the scope of applications of plasmon and hot carriers but also advanced experimental discoveries.

The timescales for hot carrier generation, emission, and transfer are very short, leading to significant challenges for fundamental study and applications. Plasmonic hot carriers function at the timescale of femtosecond to picosecond ( $<10$  ps) before thermal equilibration. In the aspect of application studies, the timescales for chemical reactions are much longer (typically a few hundred femtoseconds or above) than the lifetime of the plasmonic hot carriers. It is very important to collect hot electrons timely or/and to extend the lifetime of the hot carriers when designing plasmonic nanostructures to enable hot carriers to participate in photochemical reactions.

Indirect and direct hot electron transfer processes have been utilized to design materials and devices. Besides these processes,

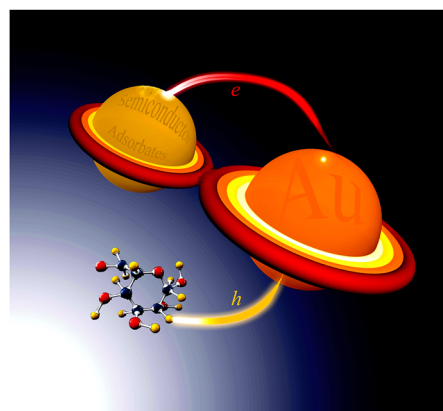


FIG. 16. Schematic illustration of the plasmonic metal nanoparticle and the hot carrier transfer.

surface catalysis, surface passivation, and heating effects may function together with plasmonic effects, which contribute to the enhanced performance of materials and devices. This complicates the separation of the role of plasmon from other effects during operation of materials and devices. As such, significant effort must be made to separate these mechanisms or effects to fully understand and utilize all these effects effectively. Indeed, several articles have presented the specific methodologies in detail for identifying and separating these mechanisms.<sup>11,15,161–163</sup>

In a plasmonic heterojunction, there are three main mechanisms of energy transfer from a plasmonic metallic nanostructure to a semiconductor or other materials,<sup>11</sup> that is, light scattering/trapping, plasmon-induced resonance energy transfer (PIRET), and hot carrier injection. It was observed from the experimental results that the hot carrier injection mechanism showed a far lower energy transfer efficiency than the other two processes. For photodetectors, chemical sensors, and bio-sensors, high signal output such as photocurrent is not that demanding. Therefore, the application of plasmonic hot electrons in these devices is promising. For plasmonic solar energy conversion devices, high photocurrent and high energy conversion efficiency are critical to commercialization of these devices. In the direct hot electron transfer pathway, the theoretical maximum efficiency is predicted to be as high as 50%. In the indirect hot electron transfer pathway, the theoretical maximum transfer efficiency is predicted to be 8%. However, in the experiments performed so far, the achieved efficiency is much lower than the theoretical maximum in both cases. Plasmonic hot electrons can be generated abundantly. However, it still remains a significant challenge in effectively harnessing plasmonic hot electrons for solar energy conversion. Theoretical understanding of plasmonic hot electron transfer, structure design, material synthesis, and interface engineering is necessary to improve the energy transfer efficiency and finally meet the demand of practical applications.

Compared with the research on plasmonic hot electrons, the studies on hot holes are limited. In reality, hot holes are equally as important as hot electrons. Few studies have shown the considerable effects of the hot hole.<sup>18,164,165</sup> Hot holes can be extracted out

and involved into photoelectrochemical processes.<sup>16,91,135–138</sup> It is interesting that plasmonic hot holes can be extracted to either an *n*-type semiconductor or a *p*-type semiconductor. After plasmonic hot holes are extracted to an *n*-type semiconductor, they can drive an oxidation reaction. After plasmonic hot holes are transferred to a *p*-type semiconductor, they can increase the open voltage and stabilize holes.<sup>137</sup> To identify the roles of hot holes and the associated mechanisms, the methods used for hot electrons can be applied to hot holes under scrutiny. More details on the applications of plasmonic hot holes can be seen in a recent review article by Tatsuma.<sup>137</sup>

Currently, the main plasmonic materials are gold and silver, which are expensive. It is necessary to develop inexpensive plasmonic materials through fundamental study and improved fabrication technology. Copper nanostructures and heavily doped semiconductors are promising candidates. Recent research has revealed that the copper nanocubes have a strong and narrow LSPR absorption band.<sup>166,167</sup> In addition, if a semiconductor is heavily doped, especially with oxygen vacancies, the free charge carrier concentration may increase to even higher than  $10^{21}$  cm<sup>-3</sup>. The doped semiconductor will then manifest SPR under visible-light or infrared-light excitation.<sup>168–170</sup> Plasmonic semiconductors can generate hot carriers by themselves. Probably, it can produce higher energy transfer efficiency in the plasmonic semiconductor–regular semiconductor heterojunctions because there may be less energy loss via the indirect transfer pathway across the interface or via the direct transfer pathway with easier orbital hybridization. Recently, plasmonic semiconductors have triggered intensive interests. Plasmonic semiconductor nanostructures based on Cu<sub>2–x</sub>S, WO<sub>3–x</sub>, and MoO<sub>3–x</sub> have been used for SERS, photocatalysis, and water splitting. However, fundamental research, device design, and fabrication of plasmonic semiconductors are just emerging.

## AUTHORS' CONTRIBUTIONS

H.T. and C.J.C. contributed equally. All authors contributed to this work and have given approval to the final version of this paper.

## ACKNOWLEDGMENTS

This work was partially supported by the Armstrong/Siadat Professorship Endowment for N.W., the Ministry of Science and Technology of Taiwan (Contract No. MOST 107-2113-M-002-008-MY3) for R.S.L., and the National Natural Science Foundation of China (Grant Nos. 51972308 and 21673245) for H.T. and Z.H., respectively.

## DATA AVAILABILITY

Data sharing is not applicable to this article as no new data were created or analyzed in this study.

## REFERENCES

- W. R. Erwin, H. F. Zarick, E. M. Talbert, and R. Bardhan, *Energy Environ. Sci.* **9**, 1577 (2016).
- C.-H. Chou and F.-C. Chen, *Nanoscale* **6**, 8444 (2014).
- M. Li, S. K. Cushing, and N. Wu, *Analyst* **140**, 386 (2015).
- X. Yang, Z. Sun, T. Low, H. Hu, X. Guo, F. J. García de Abajo, P. Avouris, and Q. Dai, *Adv. Mater.* **30**, 1704896 (2018).
- A. O. Govorov and H. H. Richardson, *Nano Today* **2**, 30 (2007).
- L. Zhou, Y. Tan, J. Wang, W. Xu, Y. Yuan, W. Cai, S. Zhu, and J. Zhu, *Nat. Photonics* **10**, 393 (2016).
- J. M. Stern, J. Stanfield, W. Kabbani, J.-T. Hsieh, and J. A. Cadeddu, *J. Urol.* **179**, 748 (2008).
- F. H. L. Koppens, T. Mueller, P. Avouris, A. C. Ferrari, M. S. Vitiello, and M. Polini, *Nat. Nanotechnol.* **9**, 780 (2014).
- C. Clavero, *Nat. Photonics* **8**, 95 (2014).
- Q. Wei, S. Wu, and Y. Sun, *Adv. Mater.* **30**, 1802082 (2018).
- N. Wu, *Nanoscale* **10**, 2679 (2018).
- Y. Zhang, S. He, W. Guo, Y. Hu, J. Huang, J. R. Mulcahy, and W. D. Wei, *Chem. Rev.* **118**, 2927 (2018).
- M. L. Brongersma, N. J. Halas, and P. Nordlander, *Nat. Nanotechnol.* **10**, 25 (2015).
- S. K. Cushing, A. D. Bristow, and N. Wu, *Phys. Chem. Chem. Phys.* **17**, 30013 (2015).
- S. K. Cushing and N. Wu, *J. Phys. Chem. Lett.* **7**, 666 (2016).
- J. S. DuChene, G. Tagliabue, A. J. Welch, W.-H. Cheng, and H. A. Atwater, *Nano Lett.* **18**, 2545 (2018).
- L. Brus, *Acc. Chem. Res.* **41**, 1742 (2008).
- X. Wu, E. S. Thrall, H. Liu, M. Steigerwald, and L. Brus, *J. Phys. Chem. C* **114**, 12896 (2010).
- C. F. Bohren, *Am. J. Phys.* **51**, 323 (1983).
- X. Li, D. Xiao, and Z. Zhang, *New J. Phys.* **15**, 023011 (2013).
- C. Voisin, N. Del Fatti, D. Christofilos, and F. Vallée, *J. Phys. Chem. B* **105**, 2264 (2001).
- J. B. Khurgin, *Nat. Nanotechnol.* **10**, 2 (2015).
- C. Frischkorn and M. Wolf, *Chem. Rev.* **106**, 4207 (2006).
- C. Zhan, X.-J. Chen, J. Yi, J.-F. Li, D.-Y. Wu, and Z.-Q. Tian, *Nat. Rev. Chem.* **2**, 216 (2018).
- S. Dal Forno, L. Ranno, and J. Lischner, *J. Phys. Chem. C* **122**, 8517 (2018).
- A. Manjavacas, J. G. Liu, V. Kulkarni, and P. Nordlander, *ACS Nano* **8**, 7630 (2014).
- M. Lisowski, P. A. Loukakos, U. Bovensiepen, J. Stähler, C. Gahl, and M. Wolf, *Appl. Phys. A: Mater. Sci. Process.* **78**, 165 (2004).
- H. Inouye, K. Tanaka, I. Tanahashi, and K. Hirao, *Phys. Rev. B* **57**, 11334 (1998).
- L.-B. Zhao, X.-X. Liu, M. Zhang, Z.-F. Liu, D.-Y. Wu, and Z.-Q. Tian, *J. Phys. Chem. C* **120**, 944 (2016).
- J. Li, S. K. Cushing, P. Zheng, T. Senty, F. Meng, A. D. Bristow, A. Manivannan, and N. Wu, *J. Am. Chem. Soc.* **136**, 8438 (2014).
- M. J. Kale, T. Avanesian, H. Xin, J. Yan, and P. Christopher, *Nano Lett.* **14**, 5405 (2014).
- Y. Tian and T. Tatsuma, *Chem. Commun.* **2004**, 1810.
- Y. Tian and T. Tatsuma, *J. Am. Chem. Soc.* **127**, 7632 (2005).
- C. Boerigter, R. Campana, M. Morabito, and S. Lincic, *Nat. Commun.* **7**, 10545 (2016).
- Q. Xiao, S. Sarina, E. R. Waclawik, J. Jia, J. Chang, J. D. Riches, H. Wu, Z. Zheng, and H. Zhu, *ACS Catal.* **6**, 1744 (2016).
- C. Boerigter, U. Aslam, and S. Lincic, *ACS Nano* **10**, 6108 (2016).
- D.-Y. Wu, X.-M. Liu, Y.-F. Huang, B. Ren, X. Xu, and Z.-Q. Tian, *J. Phys. Chem. C* **113**, 18212 (2009).
- D.-Y. Wu, L.-B. Zhao, X.-M. Liu, R. Huang, Y.-F. Huang, B. Ren, and Z.-Q. Tian, *Chem. Commun.* **47**, 2520 (2011).
- Y.-F. Huang, H.-P. Zhu, G.-K. Liu, D.-Y. Wu, B. Ren, and Z.-Q. Tian, *J. Am. Chem. Soc.* **132**, 9244 (2010).
- P. Christopher and M. Moskovits, *Annu. Rev. Phys. Chem.* **68**, 379 (2017).
- A. O. Govorov, H. Zhang, and Y. K. Gun'ko, *J. Phys. Chem. C* **117**, 16616 (2013).
- R. G. Hobbs, W. P. Putnam, A. Fallahi, Y. Yang, F. X. Kärtner, and K. K. Berggren, *Nano Lett.* **17**, 6069 (2017).

- <sup>43</sup>C. Bauer, J.-P. Abid, and H. H. Girault, *J. Phys. Chem. B* **110**, 4519 (2006).
- <sup>44</sup>C. Bauer, J.-P. Abid, D. Fermin, and H. H. Girault, *J. Chem. Phys.* **120**, 9302 (2004).
- <sup>45</sup>K. O. Aruda, M. Tagliazucchi, C. M. Sweeney, D. C. Hannah, G. C. Schatz, and E. A. Weiss, *Proc. Natl. Acad. Sci. U. S. A.* **110**, 4212 (2013).
- <sup>46</sup>R. Kostecki and J. Augustynski, *Chem. Phys. Lett.* **194**, 386 (1992).
- <sup>47</sup>R. Kostecki and J. Augustynski, *J. Appl. Phys.* **77**, 4701 (1995).
- <sup>48</sup>K. Awazu, M. Fujimaki, C. Rockstuhl, J. Tominaga, H. Murakami, Y. Ohki, N. Yoshida, and T. Watanabe, *J. Am. Chem. Soc.* **130**, 1676 (2008).
- <sup>49</sup>D. Derkacs, S. H. Lim, P. Matheu, W. Mar, and E. T. Yu, *Appl. Phys. Lett.* **89**, 093103 (2006).
- <sup>50</sup>A. Furube, L. Du, K. Hara, R. Katoh, and M. Tachiya, *J. Am. Chem. Soc.* **129**, 14852 (2007).
- <sup>51</sup>Y. Tian, X. Wang, D. Zhang, X. Shi, and S. Wang, *J. Photochem. Photobiol. A* **199**, 224 (2008).
- <sup>52</sup>L. Du, A. Furube, K. Yamamoto, K. Hara, R. Katoh, and M. Tachiya, *J. Phys. Chem. C* **113**, 6454 (2009).
- <sup>53</sup>A. Naldoni, T. Montini, F. Malara, M. M. Mróz, A. Beltram, T. Virgili, C. L. Boldrini, M. Marelli, I. Romero-Ocaña, J. J. Delgado, V. Dal Santo, and P. Fornasiero, *ACS Catal.* **7**, 1270 (2017).
- <sup>54</sup>D. C. Ratchford, A. D. Dunkelberger, I. Vurgaftman, J. C. Owrutsky, and P. E. Pehrsson, *Nano Lett.* **17**, 6047 (2017).
- <sup>55</sup>T. P. White and K. R. Catchpole, *Appl. Phys. Lett.* **101**, 073905 (2012).
- <sup>56</sup>Y. Nishijima, K. Ueno, Y. Kotake, K. Murakoshi, H. Inoue, and H. Misawa, *J. Phys. Chem. Lett.* **3**, 1248 (2012).
- <sup>57</sup>S. Mubeen, J. Lee, N. Singh, S. Krämer, G. D. Stucky, and M. Moskovits, *Nat. Nanotechnol.* **8**, 247 (2013).
- <sup>58</sup>Y. Takahashi and T. Tatsuma, *Appl. Phys. Lett.* **99**, 182110 (2011).
- <sup>59</sup>Y. K. Lee, C. H. Jung, J. Park, H. Seo, G. A. Somorjai, and J. Y. Park, *Nano Lett.* **11**, 4251 (2011).
- <sup>60</sup>L. J. Brennan, F. Purcell-Milton, A. S. Salmeron, H. Zhang, A. O. Govorov, A. V. Fedorov, and Y. K. Gun'ko, *Nanoscale Res. Lett.* **10**, 38 (2015).
- <sup>61</sup>Z. Bian, T. Tachikawa, P. Zhang, M. Fujitsuka, and T. Majima, *J. Am. Chem. Soc.* **136**, 458 (2014).
- <sup>62</sup>A. J. Leenheer, P. Narang, N. S. Lewis, and H. A. Atwater, *J. Appl. Phys.* **115**, 134301 (2014).
- <sup>63</sup>K. Wu, J. Chen, J. R. McBride, and T. Lian, *Science* **349**, 632 (2015).
- <sup>64</sup>R. Long and O. V. Prezhdo, *J. Am. Chem. Soc.* **136**, 4343 (2014).
- <sup>65</sup>A. M. Brown, R. Sundararaman, P. Narang, W. A. Goddard, and H. A. Atwater, *ACS Nano* **10**, 957 (2016).
- <sup>66</sup>A. O. Govorov and H. Zhang, *J. Phys. Chem. C* **119**, 6181 (2015).
- <sup>67</sup>L. V. Besteiro and A. O. Govorov, *J. Phys. Chem. C* **120**, 19329 (2016).
- <sup>68</sup>H. Zhang and A. O. Govorov, *J. Phys. Chem. C* **118**, 7606 (2014).
- <sup>69</sup>R. Sundararaman, P. Narang, A. S. Jermyn, W. A. Goddard, and H. A. Atwater, *Nat. Commun.* **5**, 5788 (2014).
- <sup>70</sup>M. Bernardi, J. Mustafa, J. B. Neaton, and S. G. Louie, *Nat. Commun.* **6**, 7044 (2015).
- <sup>71</sup>C. S. Kumarasinghe, M. Premaratne, Q. L. Bao, and G. P. Agrawal, *Sci. Rep.* **5**, 12140 (2015).
- <sup>72</sup>S. K. Cushing, C. J. Chen, C. L. Dong, X.-T. Kong, A. O. Govorov, R. S. Liu, and N. Wu, *ACS Nano* **12**, 7117 (2018).
- <sup>73</sup>H. M. Chen, C. K. Chen, C.-J. Chen, L.-C. Cheng, P. C. Wu, B. H. Cheng, Y. Z. Ho, M. L. Tseng, Y. Y. Hsu, T. S. Chan, J.-F. Lee, R. S. Liu, and D. P. Tsai, *ACS Nano* **6**, 7362 (2012).
- <sup>74</sup>S.-F. Hung, F.-X. Xiao, Y.-Y. Hsu, N.-T. Suen, H.-B. Yang, H. M. Chen, and B. Liu, *Adv. Energy Mater.* **6**, 1501339 (2016).
- <sup>75</sup>L. Amidani, A. Naldoni, M. Malvestuto, M. Marelli, P. Glatzel, V. Dal Santo, and F. Boscherini, *Angew. Chem., Int. Ed.* **54**, 5413 (2015).
- <sup>76</sup>K. Wu, W. E. Rodríguez-Córdoba, Y. Yang, and T. Lian, *Nano Lett.* **13**, 5255 (2013).
- <sup>77</sup>S. Link and M. A. El-Sayed, *J. Phys. Chem. B* **103**, 8410 (1999).
- <sup>78</sup>R. Berera, R. van Grondelle, and J. T. M. Kennis, *Photosynth. Res.* **101**, 105 (2009).
- <sup>79</sup>H. Nienhaus, H. S. Bergh, B. Gergen, A. Majumdar, W. H. Weinberg, and E. W. McFarland, *Appl. Phys. Lett.* **74**, 4046 (1999).
- <sup>80</sup>J. Y. Park, H. Lee, J. R. Renzas, Y. Zhang, and G. A. Somorjai, *Nano Lett.* **8**, 2388 (2008).
- <sup>81</sup>A. Hervier, J. R. Renzas, J. Y. Park, and G. A. Somorjai, *Nano Lett.* **9**, 3930 (2009).
- <sup>82</sup>J. R. Renzas and G. A. Somorjai, *J. Phys. Chem. C* **114**, 17660 (2010).
- <sup>83</sup>Z. Q. Zheng, B. Wang, J. D. Yao, and G. W. Yang, *J. Mater. Chem. C* **3**, 7067 (2015).
- <sup>84</sup>H. Nienhaus, S. J. Weyers, B. Gergen, and E. W. McFarland, *Sens. Actuators, B* **87**, 421 (2002).
- <sup>85</sup>S. Mukherjee, F. Libisch, N. Large, O. Neumann, L. V. Brown, J. Cheng, J. B. Lassiter, E. A. Carter, P. Nordlander, and N. J. Halas, *Nano Lett.* **13**, 240 (2013).
- <sup>86</sup>D. Sil, K. D. Gilroy, A. Niaux, A. Boulesbaa, S. Neretina, and E. Borguet, *ACS Nano* **8**, 7755 (2014).
- <sup>87</sup>N. Cattabiani, C. Baratto, D. Zappa, E. Comini, M. Donarelli, M. Ferroni, A. Ponzoni, and G. Faglia, *J. Phys. Chem. C* **122**, 5026 (2018).
- <sup>88</sup>F. Zhou, Q. Wang, and W. Liu, *Mater. Res. Express* **3**, 085006 (2016).
- <sup>89</sup>Y. Qiao, J. Li, H. Li, H. Fang, D. Fan, and W. Wang, *Biosens. Bioelectron.* **86**, 315 (2016).
- <sup>90</sup>Z. Kang, X. Yan, Y. Wang, Y. Zhao, Z. Bai, Y. Liu, K. Zhao, S. Cao, and Y. Zhang, *Nano Res.* **9**, 344 (2015).
- <sup>91</sup>C. Wang, X.-G. Nie, Y. Shi, Y. Zhou, J.-J. Xu, X.-H. Xia, and H.-Y. Chen, *ACS Nano* **11**, 5897 (2017).
- <sup>92</sup>T. Tsukagoshi, Y. Kuroda, K. Noda, N. Binh-Khiem, T. Kan, and I. Shimoyama, *Sensors* **18**, 399 (2018).
- <sup>93</sup>D. W. Peters, *Proc. IEEE* **55**, 704 (1967).
- <sup>94</sup>M. Y. Liu and S. Y. Chou, *Appl. Phys. Lett.* **66**, 2673 (1995).
- <sup>95</sup>W. Li and J. G. Valentine, *Nanophotonics* **6**, 177 (2017).
- <sup>96</sup>S. Faris, T. Gustafson, and J. Wiesner, *IEEE J. Quantum Electron.* **9**, 737 (1973).
- <sup>97</sup>F. Wang and N. A. Melosh, *Nano Lett.* **11**, 5426 (2011).
- <sup>98</sup>W. Wang, A. Klots, D. Prasai, Y. Yang, K. I. Bolotin, and J. Valentine, *Nano Lett.* **15**, 7440 (2015).
- <sup>99</sup>T. Gong and J. N. Munday, *Nano Lett.* **15**, 147 (2015).
- <sup>100</sup>J. B. Chou, X.-H. Li, Y. Wang, D. P. Fenning, A. Elfaer, J. Viegas, M. Jouiad, Y. Shao-Horn, and S.-G. Kim, *Opt. Express* **24**, A1234 (2016).
- <sup>101</sup>F. P. G. de Arguer, A. Mihi, and G. Konstantatos, *ACS Photonics* **2**, 950 (2015).
- <sup>102</sup>A. Sobhani, M. W. Knight, Y. M. Wang, B. Zheng, N. S. King, L. V. Brown, Z. Y. Fang, P. Nordlander, and N. J. Halas, *Nat. Commun.* **4**, 1643 (2013).
- <sup>103</sup>M. W. Knight, H. Sobhani, P. Nordlander, and N. J. Halas, *Science* **332**, 702 (2011).
- <sup>104</sup>M. A. Nazirzadeh, F. B. Atar, B. B. Turgut, and A. K. Okyay, *Sci. Rep.* **4**, 7103 (2014).
- <sup>105</sup>B. Desiatov, I. Goykhman, N. Mazurski, J. Shappir, J. B. Khurgin, and U. Levy, *Optica* **2**, 335 (2015).
- <sup>106</sup>C. Daboo, M. J. Baird, H. P. Hughes, N. Apsley, and M. T. Emeny, *Thin Solid Films* **201**, 9 (1991).
- <sup>107</sup>K. Wu, Y. H. Zhan, C. Zhang, S. L. Wu, and X. F. Li, *Sci. Rep.* **5**, 14304 (2015).
- <sup>108</sup>T. J. Echtermeyer, L. Britnell, P. K. Jasnós, A. Lombardo, R. V. Gorbachev, A. N. Grigorenko, A. K. Geim, A. C. Ferrari, and K. S. Novoselov, *Nat. Commun.* **2**, 458 (2011).
- <sup>109</sup>I. Goykhman, B. Desiatov, J. Khurgin, J. Shappir, and U. Levy, *Nano Lett.* **11**, 2219 (2011).
- <sup>110</sup>M. Casalino, M. Iodice, L. Sirleto, S. Rao, I. Rendina, and G. Coppola, *J. Appl. Phys.* **114**, 153103 (2013).
- <sup>111</sup>S. Ishii, S.-I. Inoue, R. Ueda, and A. Otomo, *ACS Photonics* **1**, 1089 (2014).
- <sup>112</sup>A. Akbari, R. N. Tait, and P. Berini, *Opt. Express* **18**, 8505 (2010).
- <sup>113</sup>I. Goykhman, B. Desiatov, J. Khurgin, J. Shappir, and U. Levy, *Opt. Express* **20**, 28594 (2012).
- <sup>114</sup>H. Chalabi, D. Schoen, and M. L. Brongersma, *Nano Lett.* **14**, 1374 (2014).
- <sup>115</sup>D. R. Ward, F. Hüser, F. Pauly, J. C. Cuevas, and D. Natelson, *Nat. Nanotechnol.* **5**, 732 (2010).
- <sup>116</sup>W. Li and J. Valentine, *Nano Lett.* **14**, 3510 (2014).

- <sup>117</sup>X. D. Gao, G. T. Fei, Y. Zhang, L. D. Zhang, and Z. M. Hu, *Adv. Funct. Mater.* **28**, 1802288 (2018).
- <sup>118</sup>A. Pescaglino, A. Martin, D. Cammi, G. Juska, C. Ronning, E. Pelucchi, and D. Iacopino, *Nano Lett.* **14**, 6202 (2014).
- <sup>119</sup>H. S. Kojori, J. H. Yun, Y. Paik, J. Kim, W. A. Anderson, and S. J. Kim, *Nano Lett.* **16**, 250 (2016).
- <sup>120</sup>H. S. Kojori, S. Cho, R. Han, J. H. Yun, J. Kim, and S. J. Kim, *J. Photonics Energy* **6**, 042509 (2016).
- <sup>121</sup>N. S. Lewis and D. G. Nocera, *Proc. Natl. Acad. Sci. U. S. A.* **103**, 15729 (2006).
- <sup>122</sup>B. O'Regan and M. Grätzel, *Nature* **353**, 737 (1991).
- <sup>123</sup>Y. H. Jang, Y. J. Jang, S. Kim, L. N. Quan, K. Chung, and D. H. Kim, *Chem. Rev.* **116**, 14982 (2016).
- <sup>124</sup>W. Ye, R. Long, H. Huang, and Y. Xiong, *J. Mater. Chem. C* **5**, 1008 (2017).
- <sup>125</sup>Y.-H. Su, Y.-F. Ke, S.-L. Cai, and Q.-Y. Yao, *Light-Sci. Appl.* **1**, e14 (2012).
- <sup>126</sup>F. P. G. de Arquer, A. Mihi, D. Kufer, and G. Konstantatos, *ACS Nano* **7**, 3581 (2013).
- <sup>127</sup>S. Mubeen, J. Lee, W.-R. Lee, N. Singh, G. D. Stucky, and M. Moskovits, *ACS Nano* **8**, 6066 (2014).
- <sup>128</sup>P. Reineck, D. Brick, P. Mulvaney, and U. Bach, *J. Phys. Chem. Lett.* **7**, 4137 (2016).
- <sup>129</sup>P. Reineck, G. P. Lee, D. Brick, M. Karg, P. Mulvaney, and U. Bach, *Adv. Mater.* **24**, 4750 (2012).
- <sup>130</sup>K. Yao, H. Zhong, Z. Liu, M. Xiong, S. Leng, J. Zhang, Y.-x. Xu, W. Wang, L. Zhou, H. Huang, and A. K.-Y. Jen, *ACS Nano* **13**, 5397 (2019).
- <sup>131</sup>D. Zhang, W. C. H. Choy, F. Xie, W. E. I. Sha, X. Li, B. Ding, K. Zhang, F. Huang, and Y. Cao, *Adv. Funct. Mater.* **23**, 4255 (2013).
- <sup>132</sup>D. Liu, D. Yang, Y. Gao, J. Ma, R. Long, C. Wang, and Y. Xiong, *Angew. Chem., Int. Ed.* **55**, 4577 (2016).
- <sup>133</sup>Y. H. Jang, Y. J. Jang, S. T. Kochuveedu, M. Byun, Z. Lin, and D. H. Kim, *Nanoscale* **6**, 1823 (2014).
- <sup>134</sup>S. D. Standridge, G. C. Schatz, and J. T. Hupp, *J. Am. Chem. Soc.* **131**, 8407 (2009).
- <sup>135</sup>A. E. Schather, A. Manjavacas, A. Lauchner, V. S. Marangoni, C. J. DeSantis, P. Nordlander, and N. J. Halas, *J. Phys. Chem. Lett.* **8**, 2060 (2017).
- <sup>136</sup>H. Nishi and T. Tatsuma, *Nanoscale* **11**, 19455 (2019).
- <sup>137</sup>T. Tatsuma and H. Nishi, *Nanoscale Horiz.* **5**, 597 (2020).
- <sup>138</sup>T. H. Peng, J. J. Miao, Z. S. Gao, L. J. Zhang, Y. Gao, C. H. Fan, and D. Li, *Small* **14**, 1703510 (2018).
- <sup>139</sup>M. Bonn, S. Funk, C. Hess, D. N. Denzler, C. Stampfl, M. Scheffler, M. Wolf, and G. Ertl, *Science* **285**, 1042 (1999).
- <sup>140</sup>Y. Zhang, T. Nelson, S. Tretiak, H. Guo, and G. C. Schatz, *ACS Nano* **12**, 8415 (2018).
- <sup>141</sup>S. Mukherjee, L. Zhou, A. M. Goodman, N. Large, C. Ayala-Orozco, Y. Zhang, P. Nordlander, and N. J. Halas, *J. Am. Chem. Soc.* **136**, 64 (2014).
- <sup>142</sup>M. J. Landry, A. Gellé, B. Y. Meng, C. J. Barrett, and A. Moores, *ACS Catal.* **7**, 6128 (2017).
- <sup>143</sup>Y. Wang, S. Wang, S. Zhang, O. A. Scherman, J. J. Baumberg, T. Ding, and H. Xu, *Nano Res.* **11**, 6384 (2018).
- <sup>144</sup>E. Pensa, J. Gargiulo, A. Lauri, S. Schlücker, E. Cortés, and S. A. Maier, *Nano Lett.* **19**, 1867 (2019).
- <sup>145</sup>X. Zhang, X. Ke, and H. Zhu, *Chem. - Eur. J.* **18**, 8048 (2012).
- <sup>146</sup>S. Yu, A. J. Wilson, J. Heo, and P. K. Jain, *Nano Lett.* **18**, 2189 (2018).
- <sup>147</sup>S. Yu and P. K. Jain, *Nat. Commun.* **10**, 2022 (2019).
- <sup>148</sup>Z. Zheng, T. Tachikawa, and T. Majima, *J. Am. Chem. Soc.* **136**, 6870 (2014).
- <sup>149</sup>U. Aslam, S. Chavez, and S. Linic, *Nat. Nanotechnol.* **12**, 1000 (2017).
- <sup>150</sup>D. F. Swearer, H. Zhao, L. Zhou, C. Zhang, H. Robotjazi, J. M. P. Martirez, C. M. Krauter, S. Yazdi, M. J. McClain, E. Ringe, E. A. Carter, P. Nordlander, and N. J. Halas, *Proc. Natl. Acad. Sci. U. S. A.* **113**, 8916 (2016).
- <sup>151</sup>L. Zhou, D. F. Swearer, C. Zhang, H. Robotjazi, H. Zhao, L. Henderson, L. Dong, P. Christopher, E. A. Carter, P. Nordlander, and N. J. Halas, *Science* **362**, 69 (2018).
- <sup>152</sup>D. F. Swearer, H. Robotjazi, J. M. P. Martirez, M. Zhang, L. Zhou, E. A. Carter, P. Nordlander, and N. J. Halas, *ACS Nano* **13**, 8076 (2019).
- <sup>153</sup>A. Primo, T. Marino, A. Corma, R. Molinari, and H. García, *J. Am. Chem. Soc.* **133**, 6930 (2011).
- <sup>154</sup>D. Ding, K. Liu, S. He, C. Gao, and Y. Yin, *Nano Lett.* **14**, 6731 (2014).
- <sup>155</sup>J. Luo, J. Chen, H. Wang, and H. Liu, *J. Power Sources* **303**, 287 (2016).
- <sup>156</sup>J. Li, S. K. Cushing, J. Bright, F. Meng, T. R. Senty, P. Zheng, A. D. Bristow, and N. Wu, *ACS Catal.* **3**, 47 (2013).
- <sup>157</sup>C. Zhen, J. C. Yu, G. Liu, and H.-M. Cheng, *Chem. Commun.* **50**, 10416 (2014).
- <sup>158</sup>S. Bai, X. Li, Q. Kong, R. Long, C. Wang, J. Jiang, and Y. Xiong, *Adv. Mater.* **27**, 3444 (2015).
- <sup>159</sup>Y. Yu, K. D. Wijesekara, X. Xi, and K. A. Willets, *ACS Nano* **13**, 3629 (2019).
- <sup>160</sup>S.-C. Lin, C.-S. Hsu, S.-Y. Chiu, T.-Y. Liao, and H. M. Chen, *J. Am. Chem. Soc.* **139**, 2224 (2017).
- <sup>161</sup>J. Li, S. K. Cushing, D. Chu, P. Zheng, J. Bright, C. Castle, A. Manivannan, and N. Wu, *J. Mater. Res.* **31**, 1608 (2016).
- <sup>162</sup>S. K. Cushing, J. Li, J. Bright, B. T. Yost, P. Zheng, A. D. Bristow, and N. Wu, *J. Phys. Chem. C* **119**, 16239 (2015).
- <sup>163</sup>S. K. Cushing, J. Li, F. Meng, T. R. Senty, S. Suri, M. Zhi, M. Li, A. D. Bristow, and N. Wu, *J. Am. Chem. Soc.* **134**, 15033 (2012).
- <sup>164</sup>E. S. Thrall, A. Preska Steinberg, X. Wu, and L. E. Brus, *J. Phys. Chem. C* **117**, 26238 (2013).
- <sup>165</sup>S. Wang, Y. Gao, S. Miao, T. Liu, L. Mu, R. Li, F. Fan, and C. Li, *J. Am. Chem. Soc.* **139**, 11771 (2017).
- <sup>166</sup>P. Zheng, H. Tang, B. Liu, S. Kasani, L. Huang, and N. Wu, *Nano Res.* **12**, 63 (2019).
- <sup>167</sup>H. Guo, Y. Chen, M. B. Cortie, X. Liu, Q. Xie, X. Wang, and D.-L. Peng, *J. Phys. Chem. C* **118**, 9801 (2014).
- <sup>168</sup>X. Liu and M. T. Swihart, *Chem. Soc. Rev.* **43**, 3908 (2014).
- <sup>169</sup>A. Agrawal, S. H. Cho, O. Zandi, S. Ghosh, R. W. Johns, and D. J. Milliron, *Chem. Rev.* **118**, 3121 (2018).
- <sup>170</sup>S. Kasani, P. Zheng, J. Bright, and N. Wu, *ACS Appl. Electron. Mater.* **1**, 2389 (2019).